

## RESEARCH ARTICLE

10.1002/2015JB012250

## Key Points:

- Tremor rate-tidal stress relation representing friction law is widely exponential
- Frictional property varies with depth, showing higher sensitivity in the shallow tremor zone
- High sensitivity appears with short-duration tremors and after large-amplitude tremors

## Supporting Information:

- Figures S1–S4

## Correspondence to:

S. Yabe,  
yabe@eps.s.u-tokyo.ac.jp

## Citation:

Yabe, S., Y. Tanaka, H. Houston, and S. Ide (2015), Tidal sensitivity of tectonic tremors in Nankai and Cascadia subduction zones, *J. Geophys. Res. Solid Earth*, 120, 7587–7605, doi:10.1002/2015JB012250.

Received 1 JUN 2015

Accepted 11 OCT 2015

Accepted article online 15 OCT 2015

Published online 7 NOV 2015

## Tidal sensitivity of tectonic tremors in Nankai and Cascadia subduction zones

Suguru Yabe<sup>1</sup>, Yoshiyuki Tanaka<sup>2</sup>, Heidi Houston<sup>3</sup>, and Satoshi Ide<sup>1</sup>

<sup>1</sup>Department of Earth and Planetary Science, University of Tokyo, Tokyo, Japan, <sup>2</sup>Earthquake Research Institute, University of Tokyo, Bunkyo, Tokyo, Japan, <sup>3</sup>Department of Earth and Space Sciences, University of Washington, Seattle, Washington, USA

**Abstract** Tectonic tremors in subduction zones, which result from slip at the deep plate interface, are known to exhibit a 12.4 h periodicity in their activity, due to tidal influence. Because tidal stress can be calculated quantitatively, the response of the plate interface can yield quantitative information about its frictional property. The relation between tremor rate and tidal stress is investigated, and an exponential relation is widely confirmed, as observed by previous studies. This study particularly focuses on spatial variations of tidal sensitivity, which are compared with spatial variations of tremor duration and amplitude. The sensitivity is quantitatively defined by the exponent of the exponential relation, which can be related to the parameter  $a\sigma$ , or  $(a - b)\sigma$  in the rate-and-state friction law, where  $\sigma$  is effective normal stress. On the shallower tremor zone, short-duration and large-amplitude tremors occur followed by more sensitive tremors. Meanwhile, deeper tremors with longer duration and smaller amplitude show lower sensitivity, although along-strike variation also exists. Typical and maximum sensitivities estimated here imply values for  $a\sigma$  or  $(a - b)\sigma$  of about 3 and 1 kPa, respectively. These correlations are consistent with a model in which the plate interface consists of a velocity-strengthening background with embedded velocity-weakening regions. The frictional heterogeneity may be statistically characterized by cluster size and density of the velocity-weakening regions and controls the overall slip behavior. The observed depth dependency of tremor duration, amplitude, and sensitivity implies that frictional heterogeneity is controlled by physical quantities varying with depth, such as temperature or fluid amount.

## 1. Introduction

In the subduction zones (SZs) around the Pacific, slow earthquakes have been detected in various frequency bands. They are composed of low-frequency earthquakes (LFEs) and tectonic tremors as an aggregation of LFEs [Shelly *et al.*, 2007a], which have major signal in 2–8 Hz [e.g., Obara, 2002], very low-frequency earthquakes (VLFs) in 20–200 s [e.g., Ito *et al.*, 2007], and slow-slip events (SSEs) in a few weeks to a few years [e.g., Dragert *et al.*, 2001], all of which are located at a deeper plate interface than interplate large earthquakes. Timing and location of these phenomena in different frequency range are closely correlated (episodic tremor and slip (ETS)) [Rogers and Dragert, 2003; Obara *et al.*, 2004; Ide and Yabe, 2014], and their focal mechanism is consistent with the geometry of plate motion [Dragert *et al.*, 2001; Ide *et al.*, 2007a; Ito *et al.*, 2007; Shelly *et al.*, 2007a; Ide and Yabe, 2014]. Therefore, slow earthquakes can be interpreted as the seismic phenomena generated by the slip on the deep plate interface, and observed signals in each frequency range (i.e., tremor, VLF, and SSE) represent the heterogeneity existing in the corresponding spatial scale.

Slow earthquakes appear to follow a different scaling relation between duration and seismic moment from that of ordinary earthquakes [Ide *et al.*, 2007b], which implies that slow earthquakes have different physics from that of ordinary earthquakes. Due to the different source physics, tectonic tremors show unique characteristics. Tremor activity recurs quasiperiodically [e.g., Rogers and Dragert, 2003; Obara *et al.*, 2004]. Such recurrence interval differs among SZs and even within an individual SZ [Idehara *et al.*, 2014]. When large tremor activities occur, tremors show diffusive migration in the along-strike direction with the speed at ~10 km/day [Ide, 2010]. The size distribution of tremors obeys an exponential law [Watanabe *et al.*, 2007; Yabe and Ide, 2014], while usually earthquakes obey a power law (i.e., Gutenberg-Richter law). The typical amplitude of tremor also varies spatially within a SZ [Yabe and Ide, 2014].

Different source physics leads to another characteristic of slow earthquakes as well, i.e., high sensitivity to small stress perturbation (around kilopascal). Since the early stage of slow earthquakes study, the sensitivity of tectonic tremors to small stress changes due to tides [e.g., Shelly *et al.*, 2007b; Rubinstein *et al.*, 2008] and

passing surface waves from distant earthquakes [e.g., Miyazawa and Mori, 2005; Rubinstein et al., 2007] has been recognized. SSEs also seem to be triggered by small stress perturbations due to passing typhoons in Taiwan [Liu et al., 2009]. Slip velocity of SSEs is modulated by tidal stress as well [Hawthorne and Rubin, 2010]. The tidal sensitivity of tremors is much stronger than the barely detectable sensitivity of some classes of ordinary earthquakes, i.e., very weak sensitivity has been detected for large earthquakes [e.g., Tsuruoka et al., 1995; Cochran et al., 2004] and seismicity before large earthquakes [Tanaka, 2010, 2012]. The strong tidal response of tremors is thought to be due to near-lithostatic pore fluid pressure [e.g., Shelly et al., 2006; Audet et al., 2009].

Because the tidal sensitivity of tremor reflects how the plate interface slips in response to a known stress change, it has implications for the frictional property on the plate interface. Tidal sensitivity of tremor was first recognized by the frequency of tremor/LFE catalogs [Shelly et al., 2007b; Rubinstein et al., 2008]. Spectral analysis of such catalogs usually shows high amplitudes at the frequency of the M2 tide (~12.4 h period), which is the largest constituent in tidal components. Spatial variation of tidal sensitivity was discussed by comparing spectrum amplitude of tremor catalogs at this frequency [Ide, 2010, 2012]. However, the study of tidal sensitivity can be more quantitative because tidal sensitivity is the response of plate interface to known stress change. Nakata et al. [2008] explained the phase delay of tremor activities to tidal stress by rate-and-state friction law (RSF) [Dieterich, 1994] and estimated frictional property in RSF. Thomas et al. [2009] estimated effective frictional coefficient with the assumption that maximum tidal sensitivity should be realized and showed that frictional coefficient is very small ( $<0.1$ ).

Recent studies [Thomas et al., 2012; Beeler et al., 2013; Ide and Tanaka, 2014; Houston, 2015] found exponential relations between tremor rate and tidal stress. Assuming that tremor rate is proportional to background slip rate, this means slip velocity is proportional to exponential of stress; that is, these relations represent frictional law in a slow-earthquake region. Thomas et al. [2012] and Beeler et al. [2013] investigated tectonic tremors in San Andreas Fault and found an exponential relation between tremor rate and tidal shear stress. Beeler et al. [2013] examined dislocation creep, dislocation glide, and RSF to explain the relation and interpreted this exponential relation as the direct effect of RSF. Ide and Tanaka [2014] investigated an isolated tremor cluster in Nankai SZ, which is very sensitive to tide, and found an exponential relation between tremor rate and tidal level recorded at a nearby tide gauge. They interpreted this relation as an RSF-type rate-strengthening friction law. Houston [2015] investigated tremors in large ETS episodes in Cascadia SZ and found that tremors in the early and intermediate stage of ETS do not show tidal sensitivity, whereas tremor rate in the later stage of ETS is an exponential function of the calculated tidal stress. She interpreted this relation as a Weibull-type friction law and that temporal change of tidal sensitivity is due to the slip weakening of the plate interface by SSE.

This study investigates the tidal sensitivity of tectonic tremors in Nankai and Cascadia SZs. We particularly focus on the spatial variations of tidal sensitivity because previous studies were spatially limited or averaged. The estimation of spatial variation of tidal sensitivity enables comparison with the spatial variation of tremor duration and amplitude, which were estimated by Yabe and Ide [2014]. The spatial variation of the two latter properties should also reflect the heterogeneity on the plate interface. Hence, comparison of these characteristics will be helpful to understand the physics of slow earthquakes. In section 2, we first present analysis methods for tidal stress calculation, describe the categorization of tremors into “initiation,” “front,” and “later” groups, and estimate tidal sensitivity using the maximum likelihood method. In the next section, spatial distributions of the estimated tidal sensitivity are shown, and they are compared with duration and amplitude of tremor. Finally, we discuss how a frictional property can be estimated from tidal sensitivity of tremors and present a qualitative physical model of slow earthquakes in the last section.

## 2. Analysis Method

### 2.1. Tidal Stress Calculation

In the tidal stress calculation, both body tide and ocean tide are estimated [e.g., Tsuruoka et al., 1995]. First, the stress tensor is calculated every  $0.1^\circ$  grid along the plate interface [Baba et al., 2002; Nakajima and Hasegawa, 2007; and Hirose et al., 2008, for Nankai SZ and McCrory et al., 2012, for Cascadia SZ]. The tidal potential of Tamura [1987] is used to calculate the body tide. Ocean height change is calculated using Some Programs for Ocean-Tide Loading (SPOTL) [Agnew, 2012] with ocean models in Table 1 for ocean tide.

Region	Short-period constituents	Long-period constituents
Nankai	<i>Guo et al. [2010]</i> <i>Matsumoto et al. [2000]</i>	<i>Matsumoto et al. [2000]</i>
Cascadia	<i>Egbert and Erofeeva [2002]</i> <i>Savcenko and Bosch [2012]</i>	<i>Savcenko and Bosch [2012]</i>

Green's function is calculated by the method of *Okubo and Tsuji [2001]* with preliminary reference Earth model (PREM) structure [*Dziewonski and Anderson, 1981*]. Then, the tidal stress tensor is converted to traction on the fault using dip, strike, and rake on the plate interface. A detailed description of the calculation is provided in Appendix A.

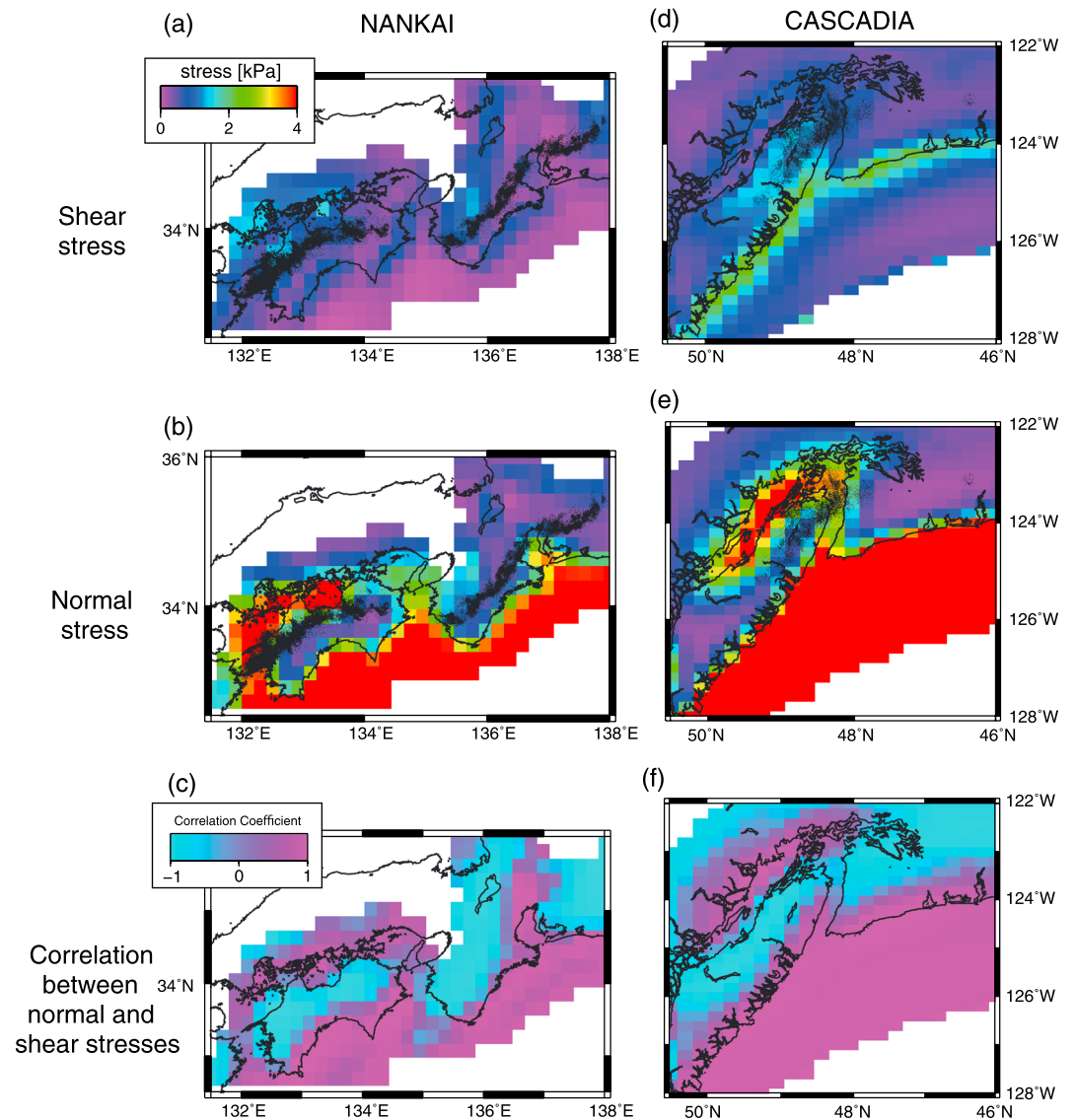


**Figure 1.** Map view of calculated tidal stress in Nankai and Cascadia subduction zones. (a) Shear stress distribution in the Nankai subduction zone. The color represents the RMS amplitude of tidal shear stress on the plate interface. The color scale is common for Figures 1a, 1b, 1d, and 1e. The distributions of detected tremor events used for analysis are shown by black dots. (b) Same as Figure 1a, but for tidal normal stress. (c) The correlation coefficient between tidal normal stress and tidal shear stress is shown. They are correlated in offshore regions, while they are anticorrelated in onshore regions. (d) Same as Figure 1a, but for the Cascadia subduction zone. (e) Same as Figure 1b, but for the Cascadia subduction zone. (f) Same as Figure 1c, but for the Cascadia subduction zone.

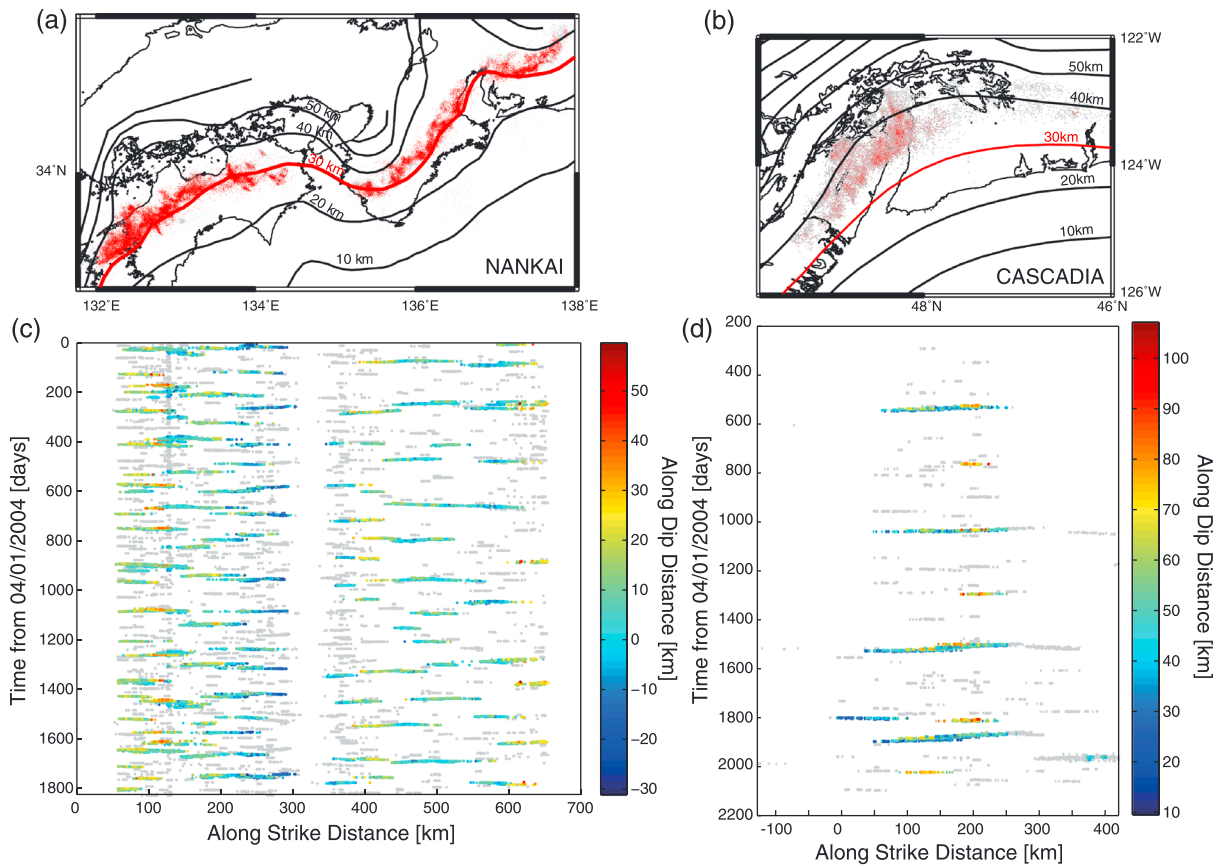


**Figure 2.** Map and time plot of detected tremor events in Nankai and Cascadia subduction zones. (a) Tremor distributions in the Nankai subduction zone detected by *Yabe and Ide* [2014] are shown in map view. Gray dots are all tremors in the catalog, and red dots are tremors used in the analysis. Plate models by *Baba et al.* [2002], *Nakajima and Hasegawa* [2007], and *Hirose et al.* [2008] are also shown. (b) Same as Figure 2a, but for the Cascadia subduction zone. Plate model is by *McCroly et al.* [2012]. (c) Time plot of tremors in the Nankai subduction zone. The horizontal axis is along-strike distance, which is calculated using curvilinear coordinate along 30 km depth of the plate model (red line in Figure 2a). Gray dots are all tremors in the catalog, and colored dots are tremors used in the analysis, which are color coded by along-dip distance, which is also measured from 30 km depth contour. (d) Same as Figure 2c, but for the Cascadia subduction zone.

In Figure 1, spatial distributions of RMS amplitudes of tidal shear stress and normal stress calculated for 10 years from April 2004 are shown for each SZ. Because both SZs have an inland sea, where tidal sea level change is much larger than the outer Pacific Ocean, tidal stress distribution is highly heterogeneous. In Nankai SZ, the bending plate geometry (Figure 2) also contributes to the complication of tidal stress distribution. The amplitude of normal stress is usually larger than shear stress beneath the sea, but comparable beneath land. In general, tidal shear stress and tidal normal stress are correlated at offshore regions and anticorrelated at onshore regions (Figures 1c and 1f). Around the coastline, the relation between them is complex.

### 2.2. Tremor Clustering

In this study, tremor catalogs in Nankai and Cascadia SZs constructed by *Yabe and Ide* [2014] with the envelope correlation method are utilized. The duration of tremors ranges from 10 s to 300 s. The period of catalog is from April 2004 to March 2009 in Nankai SZ and from January 2005 to December 2009 in Cascadia SZ. *Houston* [2015] analyzed tremors in large ETs in Cascadia SZs and found that tidal sensitivity appears in tremors in the later stage of ETs. Hence, this study also categorizes tremors in large tremor activities into initiation, front, and later tremors.

First, tremors in the catalogs are grouped into clusters by connecting tremor pairs within 2 days and 20 km. These values are adopted based on the typical duration and length of minor (i.e., inter-ETS) tremor activities. We only look at large clusters within which more than 200 events are contained and call them ETs in this study. There were 107 such ETs in Nankai SZ and 13 in Cascadia SZ. In Figure 2, all tremors in the catalogs and selected tremors in ETs defined above are shown.

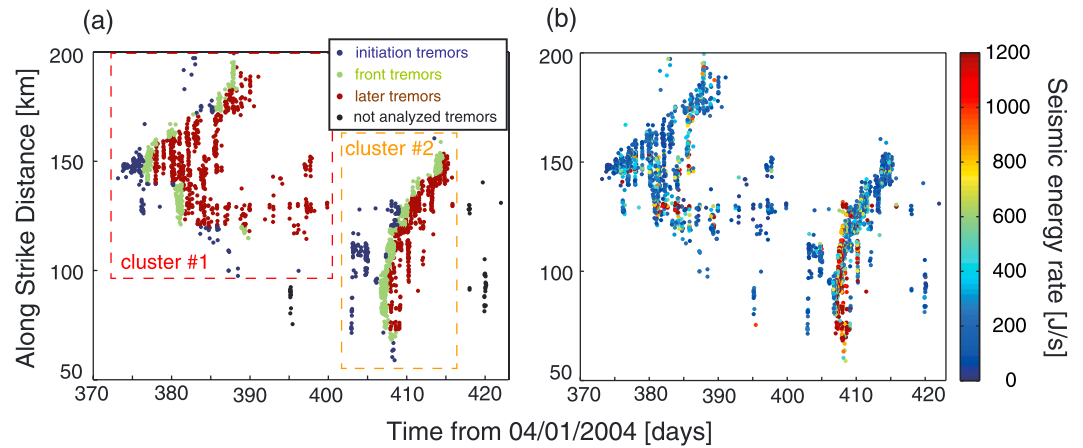


**Figure 3.** An example of tremor categorization in the Shikoku region. A portion of time plot of tremors (Figure 2a) in Shikoku region is shown. (a) Colors of dots represent the type of tremors (blue: initiation, green: front, and red: later). (b) The same time plot as Figure 3a, but colors of dots represent seismic energy rate (amplitude) estimated by *Yabe and Ide* [2014].

Then, tremors in ETSs are divided into three categories. Here, we define the along-strike coordinate as the curvilinear coordinate along 30 km depth of the slab model (Figure 2). In each along-strike bin of 10 km width, we measure the number of events per day every 0.1 days. We define the front stage of ETS as 24 h starting when the tremor rate first exceeds 20 events per day in the bin. This rate is determined empirically so that tremors increasing their amplitude after the initiation of ETS are categorized into front tremors. Tremors within this 1 day period are categorized as front tremors. Initiation tremors are defined as tremors occurring before the front stage, and later tremors occur after the front stage. The initiation and front stages in this study are analogous to the “initial” stage in *Houston* [2015]. An example of categorization of tremors in the Shikoku region is shown in Figure 3.

### 2.3. Tidal Sensitivity Estimation

We investigate the spatial distributions of tidal sensitivity of tremor, for every 0.1° grid point in latitude and longitude. Tremors with epicenters within 20 km from each grid point are considered. We compare tremor activity only with tidal shear stress because previous studies suggest that friction coefficient is very small in the tremor region and insensitive to normal stress [e.g., *Thomas et al.*, 2009, 2012; *Houston*, 2015]. We also assume here that the relation between tremor rate and tidal shear stress is exponential as

$$R(\tau) = R_0 \exp(\alpha\tau) \quad (1)$$

because such a relation is suggested by observational studies [*Thomas et al.*, 2012; *Beeler et al.*, 2013; *Ide and Tanaka*, 2014; *Houston*, 2015] and theoretical analysis of a simple spring-block system with RSF [*Ader et al.*, 2012], and in fact, our data fit it (Figure S1 in the supporting information). In equation (1),  $R$  is the tremor rate,  $R_0$  is a reference tremor rate when tidal shear stress is zero,  $\tau$  is the tidal shear stress, and the parameter  $\alpha$  represents tidal sensitivity. We estimate this parameter  $\alpha$  using the maximum likelihood method.

The maximum likelihood method for this problem is formulated as follows. Tremor rate is proportional to the probability of tremor occurrence per unit time, obeying exponential law as

$$P(t) \propto R(\tau(t)) \propto \exp(\alpha\tau(t)) \quad (2)$$

The probability of tremor occurrence at tidal stress  $\tau$  can be expressed as

$$P(\tau) = QT(\tau)\exp(\alpha\tau) \quad (3)$$

where  $T(\tau)$  is the time distribution density function and  $Q$  is normalized factor, which is expressed as

$$Q^{-1} = \int_{\tau_{\min}}^{\tau_{\max}} T(\tau)\exp(\alpha\tau) d\tau \quad (4)$$

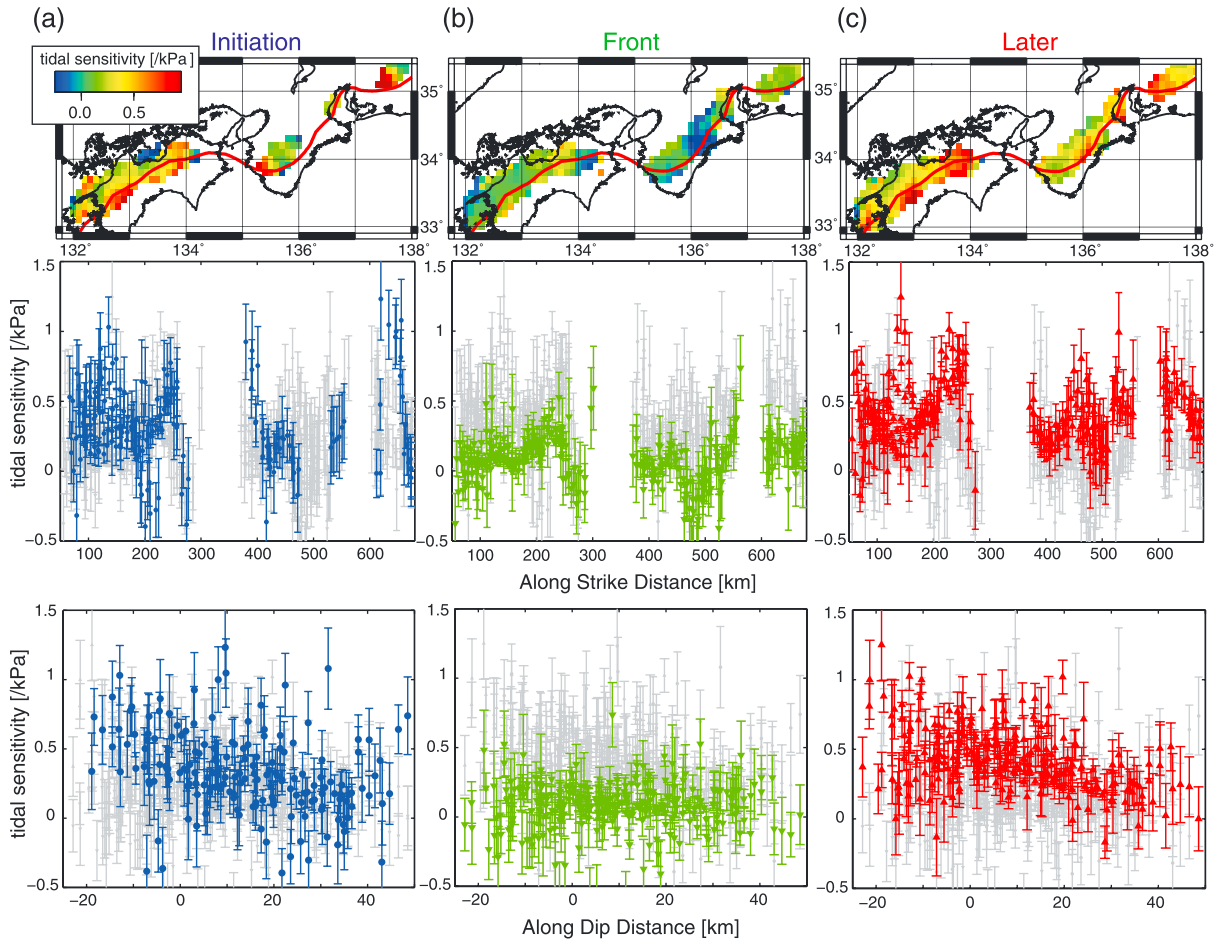


**Figure 4.** Spatial distribution of tidal sensitivity in the Nankai subduction zone. (a) The top panel shows the tidal sensitivity of initiation tremors in map view. Only estimations with uncertainty  $\Delta\alpha < 0.3 \text{ kPa}^{-1}$  are shown. The color shows tidal sensitivity. The red line represents the 30 km depth contour of the plate model, which is the reference line for along-dip distance. The middle panel shows the tidal sensitivity of each grid point versus along-strike distance (kilometer) at the grid point. Blue symbols represent tidal sensitivity of initiation tremors at each grid point, while gray symbols show results for all three types of tremor. In the bottom panel, tidal sensitivity of each grid point is plotted against along-dip distance in the same manner as the middle panel. (b) Same as Figure 4a, but for front tremors. (c) Same as Figure 4a, but for initiation tremors.

The variables  $\tau_{\min}$  and  $\tau_{\max}$  in equation (4) are the minimum and maximum of tidal shear stress at the location. In the observed data,  $N$  tremors occurred when tidal stress is  $\tau_1, \dots, \tau_N$ . Such probability can be expressed as follows:

$$\log\{L(\alpha|\tau_1, \dots, \tau_N)\} = \sum_{i=1}^N \log(T(\tau_i)) + \alpha \sum_{i=1}^N \tau_i - N \log \left\{ \int_{\tau_{\min}}^{\tau_{\max}} T(\tau) \exp(\alpha\tau) d\tau \right\} \quad (5)$$

Likelihood  $L$  of equation (5) becomes its maximum when the parameter  $\alpha$  satisfies

$$\frac{\int_{\tau_{\min}}^{\tau_{\max}} \tau T(\tau) \exp(\alpha\tau) d\tau}{\int_{\tau_{\min}}^{\tau_{\max}} T(\tau) \exp(\alpha\tau) d\tau} = \frac{\sum_{i=1}^N \tau_i}{N} \quad (6)$$

We solve equation (6) numerically to estimate the parameter  $\alpha$ . After estimating  $\alpha$ ,  $R_0$  in equation (1) can be calculated as  $NQ/T_0$ , where  $T_0$  is the total period of tremor activity.

The uncertainty in the estimated parameter  $\alpha$  can be assessed from equation (5). When the likelihood at its maximum,  $\partial \log(L)/\partial \alpha$  is zero, but  $\partial^2 \log(L)/\partial \alpha^2$  is not. Because  $\Delta \log(L) = 2$  corresponds to the 95%

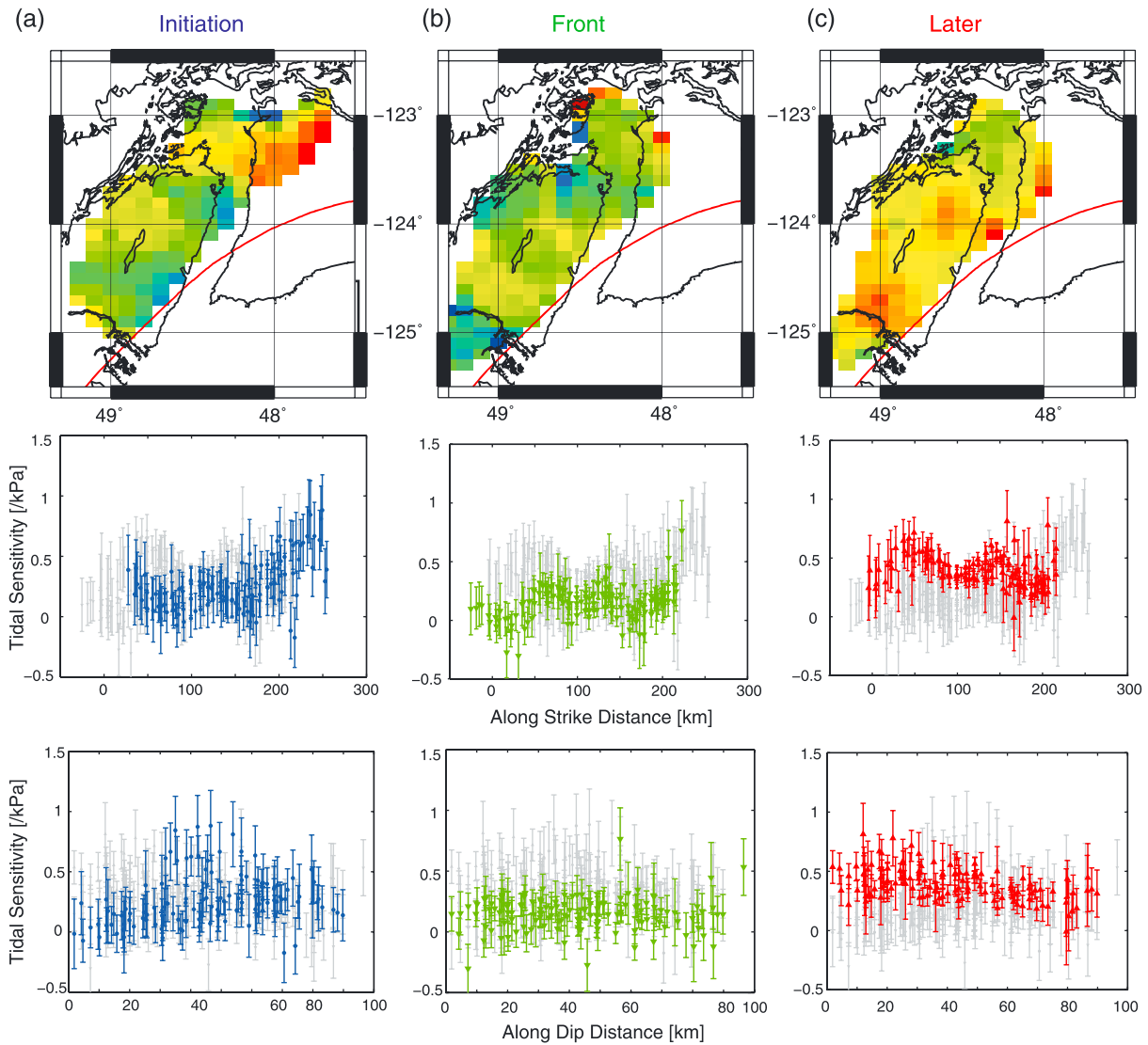


**Figure 5.** Spatial distribution of tidal sensitivity in the Cascadia subduction zone. (a) The top panel shows tidal sensitivity of initiation tremors in map view. Only estimations with uncertainty  $\Delta\alpha < 0.3 \text{ kPa}^{-1}$  are shown. The color shows tidal sensitivity. The red line represents 30 km depth contour of plate model, which is the reference line for along-dip distance. The middle panel shows tidal sensitivity of each grid point versus along-strike distance (kilometer) at the grid point. Blue symbols represent tidal sensitivity of initiation tremors at each grid point, while gray symbols show results for all three types of tremor. In the bottom panel, tidal sensitivity of each grid point is plotted against along-dip distance in the same manner as the middle panel. (b) Same as Figure 5a, but for front tremors. (c) Same as Figure 5a, but for initiation tremors.

confidence interval for a Gaussian distribution, the uncertainty in the estimated parameter  $\alpha$  can be expressed as follows.

$$\Delta\alpha = 2 \left| \frac{\partial^2 \log(L)}{\partial \alpha^2} \right|^{-1/2} \quad (7)$$

Examples of estimated tremor relation (1) are shown in Figure S1, with a plot of tremor rate and tidal stress. We can confirm that the exponential model can fit the data well.

### 3. Estimated Tidal Sensitivity

In Figures 4 and 5, spatial distribution of tidal sensitivity is shown for Nankai and Cascadia SZs, respectively, for initiation, front, and later tremors. These are selected reliable estimations with small uncertainty

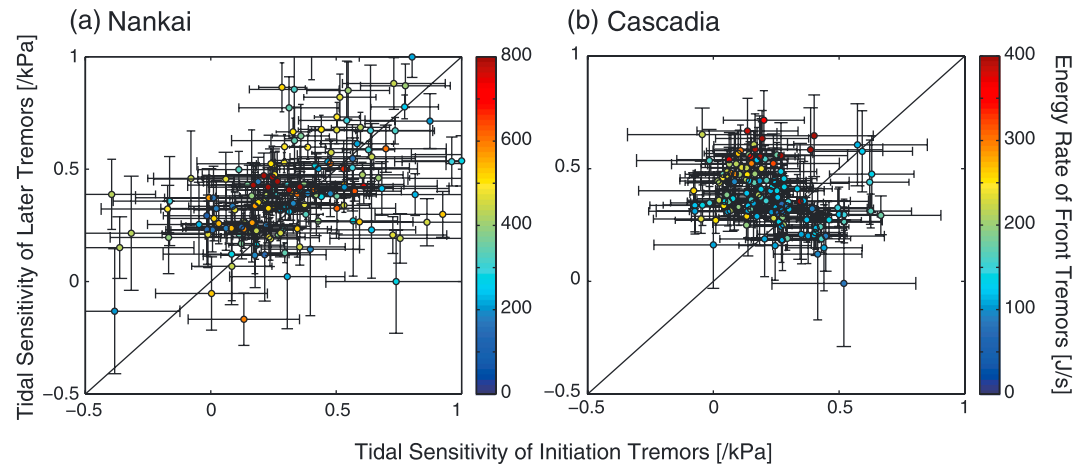


**Figure 6.** Comparison of tidal sensitivity between initiation and later tremors. (a) Tidal sensitivity of initiation tremors (horizontal axis) at each grid point is compared with that of later tremors (vertical axis). The color of symbols represents the amplitude of front tremors at the grid point, which are measured as the median value of seismic energy rate of tremors in the grid estimated by *Yabe and Ide* [2014]. (b) Same as Figure 6a, but for the Cascadia subduction zone.

( $\Delta\alpha < 0.3 \text{ kPa}^{-1}$ ). We can identify some regions of high sensitivity, such as in western Shikoku, where *Shelly et al.* [2007b] found strong sensitivity, and in eastern Shikoku. Sensitivity is relatively low in the Kii region of Nankai SZ. These features are consistent with the spatial variation of tidal sensitivity in Figure 13 of *Ide* [2012], who investigated tidal sensitivity of tremors using a frequency-based method, without categorizing initiation, front, and later tremors. In Cascadia SZ, sensitivity is generally lower than Nankai SZ. However, there are some regions with locally high sensitivity, such as around  $48.5^\circ\text{N}, 124^\circ\text{W}$  and around  $47.8^\circ\text{N}, 123.2^\circ\text{W}$ . The former is consistent with the result of *Ide* [2012]. In Figure 1 of *Houston* [2015], both regions are observed as high-consistency regions where a large portion of tremors occur when tidal stress is positive (i.e., tidal-sensitive regions). The latter area is also roughly consistent with the initiation area of ETSS [Houston, 2015]. *Royer et al.* [2015] also investigate tidal sensitivity of many families of LFEs detected in Cascadia SZ. They describe LFE families around  $48.5^\circ\text{N}, 124^\circ\text{W}$  as tidal-sensitive ones, which is consistent with our result. However, tidal sensitivity of LFE families is not so high around  $47.8^\circ\text{N}, 123.2^\circ\text{W}$ . Rather, in their study, LFE families around  $48.0^\circ\text{N}, 123.2^\circ\text{W}$  show high sensitivity, where our result shows higher sensitivity.

Generally, front tremors are less sensitive to tidal stress, which is consistent with the observation by *Houston* [2015]. Figure 6 compares tidal sensitivities for initiation and later tremors. In Nankai SZ, initiation tremors also show tidal sensitivity comparable to later tremors. In Cascadia SZ, initiation tremors in most regions do not show tidal sensitivity, whereas later tremors show higher sensitivity. Average sensitivities for each stage and each SZ are shown in Table 2.

In addition to the along-strike variation, we observe along-dip variation (Figures 4 and 5). In Nankai SZ, initiation and later tremors show higher sensitivity in shallower regions, whereas deeper tremors are less sensitive. In Cascadia SZ, only later tremors show higher sensitivity in shallower regions. Front tremors are insensitive for all depths in both SZs. When we apply linear regression analysis to confirm these trends considering the estimation uncertainty of tidal sensitivity, we obtain slopes of  $-6 \pm 3 \text{ Pa}^{-1} \text{ km}^{-1}$  (3 sigma),  $-5 \pm 2 \text{ Pa}^{-1} \text{ km}^{-1}$ , and  $-3 \pm 2 \text{ Pa}^{-1} \text{ km}^{-1}$  for initiation tremors in Nankai SZ, later tremors in Nankai SZ, and later tremors in Cascadia SZ, respectively, with the assumption that standard variation for fitting data is on the same order of uncertainty in the tidal sensitivity estimation ( $0.2 \text{ kPa}^{-1}$ ).

**Table 2.** Average Sensitivity  $\alpha$  ( $\text{kPa}^{-1}$ ) in Equation (1) During Each Stage for Each Subduction Zone

Stage	Definition	Nankai	Cascadia
Initiation tremors	Before front period	0.33	0.25
Front tremors	First day exceeding 20 tremors per day	0.08	0.16
Later tremors	After front period	0.41	0.38

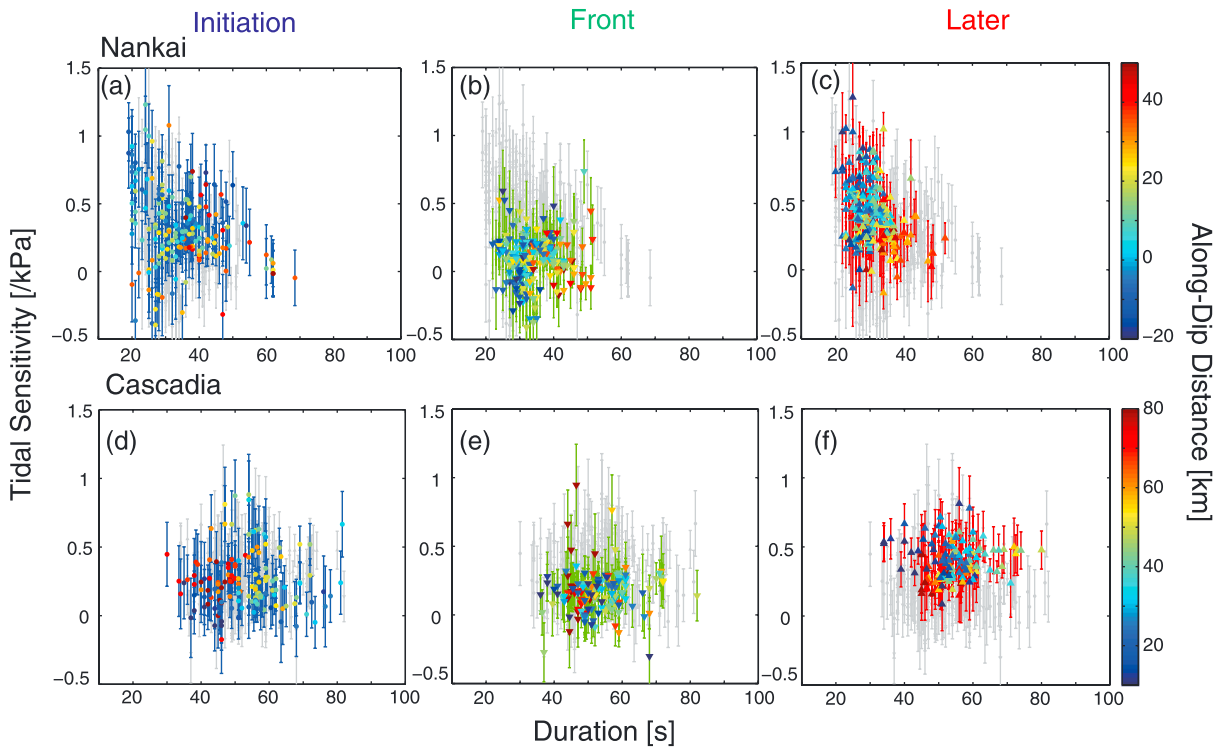


**Figure 7.** Dependence of tidal sensitivity on tremor duration in the Nankai and Cascadia subduction zones. Tidal sensitivity at each grid point from Figures 4 and 5 is shown versus duration of tremors, which was defined as the median value of durations of tremors in the grid estimated by *Yabe and Ide* [2014]. The color of dots represents along-dip distance of the grid point. (a) For initiation tremors in the Nankai subduction zone. (b) For front tremors in the Nankai subduction zone. (c) For later tremors in the Nankai subduction zone. (d) For initiation tremors in the Cascadia subduction zone. (e) For front tremors in the Cascadia subduction zone. (f) For later tremors in the Cascadia subduction zone.

Figure 7 compares estimated tidal sensitivity with the duration of tremor signals estimated by *Yabe and Ide* [2014], which is defined as the half-value width of a tremor envelope [*Ide*, 2010, 2012]. The typical duration for each grid point is defined as the median value of durations of tremors used for the tidal sensitivity analysis. Comparing duration of tremors in Nankai SZ with that in Cascadia SZ, Nankai SZ generally has a shorter duration. Initiation and later tremors with shorter durations, which are concentrated in Nankai SZ, tend to have higher sensitivity, and it decreases with duration. Meanwhile, tremors with longer duration in Cascadia SZ tend to show lower sensitivity and do not show dependency to duration of tremors. As a whole, there seems to exist a tendency that shorter tremors tend to show higher sensitivity, while longer tremors tend to show lower sensitivity. This tendency was also suggested by *Ide* [2010, 2012]. Along-dip dependency of duration can be confirmed here as well by the color scale of Figure 7 (also see Figure S2a). In contrast, *Thomas et al.* [2012] found that tidal sensitivity is higher in deeper LFEs and lower in shallower LFEs in San Andreas Fault.

*Yabe and Ide* [2014] estimated the amplitude of tremors at each grid point as the median value of seismic energy rates of tremors. Amplitudes of tremors vary spatially, and shallower tremors tend to be larger (Figure S2b) [Figure 7 of *Yabe and Ide*, 2014]. As *Yabe and Ide* [2014] pointed out and as can be seen in Figure 3, the initiation stage of ETSs begins with small-amplitude tremors, followed by a large-amplitude tremor burst with high tremor rate in the front stage. The amplitude of tremors in the front stage seems to influence the tidal sensitivity of the later stage. Figure 8 compares the energy rate of front tremors with the tidal sensitivity of later tremors and along-dip distance at all grid points. On the deeper part of the ETS zone, only small-amplitude tremors occur in the front stage followed by less tidal-sensitive tremors in the later stage. Meanwhile, on the shallower part, various amplitude tremors occur in the front stage followed by higher tidal-sensitive tremors in the later stage (also see Figure S2b for along-dip dependency of tremor amplitude). Especially in Cascadia SZ, tidal sensitivity tends to increase from the initiation stage to later stage in the region where energetic tremors occur in the front stage of ETS (Figure 6).

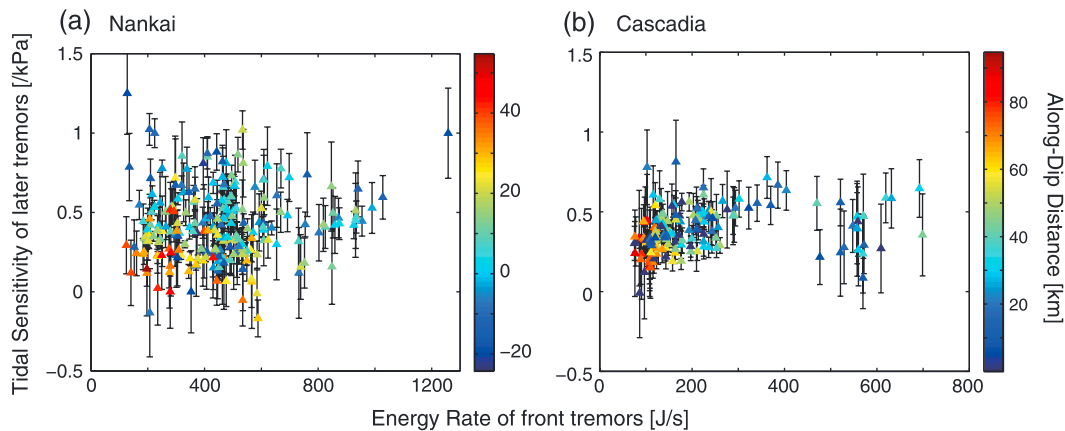


**Figure 8.** Tremor amplitude dependency of tidal sensitivity in the Nankai and Cascadia subduction zones. Tidal sensitivity of later tremors at each grid point from Figures 4 and 5 is shown versus amplitude of front tremors at the grid point, which was defined as the median value of seismic energy rate of tremors in the grid estimated by *Yabe and Ide* [2014]. The color of dots represents along-dip distance at the grid point. (a) For the Nankai subduction zone. (b) For the Cascadia subduction zone.

Tidal sensitivity does not show significant dependence on the variation of tidal shear stress measured with RMS amplitude, although a weak negative correlation might exist (Figure S3). The uncertainty in the estimation is large when the stress variation is small. Although some correlations exist among the variability of tidal stress, duration, and amplitude of tremors (Figure S4), it is not obvious to derive general relationships for three stages of tremor in two subduction zones.

## 4. Discussions

### 4.1. Reliability of Tidal Sensitivity Estimation

In tremor analysis, some criteria have been used (such as criteria for tremor clustering of 2 days and 20 km). Ideally, these clustering and categorizing of tremor activities should be done using the technique of seismic statistics [for example, epidemic-type aftershock sequence model for ordinary earthquakes; *Ogata*, 1983], which is not done by this study. Hence, the uncertainty of the estimation might be larger than values estimated in the maximum likelihood method. However, we observe common features in spatial distribution of tidal sensitivity with previous studies with frequency-based method [*Shelly et al.*, 2007b; *Ide*, 2012]. A negative correlation between tidal sensitivity and duration of tremor is also observed by *Ide* [2012]. These coincidences suggest that the uncertainty in our estimation is not so large that results presented here would be changed by the uncertainty.

In this analysis, we only compare tidal shear stress with tremor activities because frictional coefficient in slow-earthquake regions seems to be very small [e.g., *Thomas et al.*, 2009, 2012; *Houston*, 2015]. A wide area shows a positive correlation between tidal shear stress and tremor activities, which suggests that our assumption is basically valid. However, in some cases, it is better to consider coulomb stress rather than shear stress only. For example, a wide negative-correlation patch exists in front tremors of the Kii region. In this region, tidal shear stress roughly anticorrelates with tidal normal stress (Figure 1c). Therefore, a negative correlation with tidal shear stress might suggest a positive correlation with tidal normal stress in this region, although we need further analysis to make it clear.

### 4.2. Estimated Frictional Parameter

Tidal effect on the fault is investigated in some previous studies [*Ader et al.*, 2012; *Beeler et al.*, 2013; *Hawthorne and Rubin*, 2013]. *Ader et al.* [2012] especially focused on time period dependency of slip velocity response of a spring slider following RSF to harmonic stress perturbations. They found that induced velocity changes depend exponentially on the stress perturbation if the period falls within two specific ranges related to the characteristic timescale for the evolution of the state variable,  $T_\theta$ .  $T_\theta = 2\pi D_c / V_{ss}$  where  $V_{ss}$  is the steady state velocity and  $D_c$  is the characteristic slip distance for friction to evolve between two steady states. If the time period of perturbation is longer than this timescale, the state variable can change and a quasisteady state is realized. Meanwhile, if the time period of perturbation is shorter than the characteristic timescale,

the state variable does not change, and only direct effect works. In the context of this Ader et al. model, because we observe exponential behavior quantified by the sensitivity  $\alpha$  in our equation (1), one of two situations must pertain: either the dominant period of oscillation must lie in a specific period range much larger than  $T_\theta$  in which case  $V/V_{ss} = \exp[\Delta\tau/(a-b)\sigma]$ , or it must be less than  $T_\theta$  in which case  $V/V_{ss} = \exp[\Delta\tau/a\sigma]$ . Thus, assuming the exponential relation in our observation represents RSF, in the first case, our observations of  $\alpha$  can constrain  $(a-b)\sigma$  and, in the second,  $a\sigma$ .

Appropriate values of  $V_{ss}$  are not well known for ETSs in the slow-slip region and likely decrease as slip accumulates at a point during ETS. In the later stage of an ETS,  $V_{ss}$  is probably still well above its long-term inter-ETS value. We considered a range of values for  $V_{ss}$  from  $10^{-8}$  to  $10^{-7}$  m/s based on estimates in Rubin [2011]. Nor are appropriate values of  $D_c$  known for the slow-slip environs or even for natural crustal faults. We considered  $D_c$  ranging from 2 to 500  $\mu\text{m}$  [Dieterich, 1978; Marone, 1998]. These values yield  $T_\theta$  ranging from 0.015 to 3.6 days. The dominant tidal period of 12.4 h falls within that range, so with this model it is not clear whether our results for  $\alpha$  can be interpreted as  $\alpha^{-1} \sim (a-b)\sigma$  or  $\alpha^{-1} \sim a\sigma$ . If we assume that  $a$  or  $a-b$  is of the order 0.01, effective normal stress  $\sigma$  would be of the order 0.3 MPa, which suggests the presence of near-lithostatic fluid pressure.

Note that the frictional parameter inferred in this study represents only a macroscopic property of friction. A small region with negative  $a-b$  is required to accelerate slip and radiate seismic signals. The accelerated slip must be decelerated by the surrounding velocity-strengthening region so as not to grow further into a large earthquake. Thus, as a whole, the frictional property estimated in this study suggests velocity strengthening.

### 4.3. Implications for Physics of Slow Earthquakes

Key features observed in the previous section are (i) the tremor region macroscopically has an exponential-type velocity-strengthening friction law, (ii) shorter-duration tremors tend to have higher tidal sensitivity, and (iii) ETS starts with small-amplitude tremors (initiation tremors) followed by large-amplitude tremors (front/late tremors). Large-amplitude front tremors are insensitive to tides, whereas tremors in the later stage of ETS have higher tidal sensitivity, and (iv) tidal sensitivity, duration, and amplitude of tremors are dependent on the downdip position. These observations can be interpreted with the model of Ando et al. [2010, 2012] and Nakata et al. [2011], which we call the Ando model, in terms of cluster size and density of velocity-weakening regions, which characterize the frictional heterogeneity on the plate interface, as explained below.

In the Ando model, microscopic velocity-weakening regions are embedded in the velocity-strengthening background [Figure 5 of Ando et al., 2012] (Figure 9a). Tremors and slow slips occur as a result of the successive breakage of velocity-weakening regions interacting with the surrounding velocity-strengthening background. This heterogeneous frictional distribution is statistically characterized by two quantities: cluster size and density. Because velocity-weakening regions cannot interact directly beyond the size of cluster, due to their separation by the velocity-strengthening background region, slip expands slowly compared to seismic slip, and quasiconstant moment rate [Ide et al., 2007b], which is a fundamental characteristic of slow earthquakes, is reproduced. The density of velocity-weakening regions within the cluster size controls the local strength of the fault. The variation in the cluster size and density of the velocity-weakening region results in various characteristics of tremors. For example, a larger cluster size and higher density will result in longer-duration and larger-amplitude tremors [Nakata et al., 2011], respectively. The higher-density region, which can bear higher stress accumulation, can also reproduce local speedup of tremor migrations, which are called rapid tremor reversals (RTR) [Houston et al., 2011].

The first key feature of our observations, the general prevalence of velocity strengthening, is consistent with the assumption of background in the Ando model. However, Ando et al. [2012] suggested a Newtonian viscosity type of friction law to reproduce diffusive migration of tremors, while we obtain an exponential friction law. Further studies will be necessary to understand this apparent contradiction. Although we assume exponential function as friction law (RSF), and it fits the data well (Figure S1), some other function of an Arrhenius-type creep law might be able to explain the data as well. Beeler et al. [2013] examined three types of creep law, dislocation creep, dislocation glide, and RSF, to explain the relation between tidal stress and LFE rate in San Andreas Fault. They found that only RSF could explain the data with plausible physical quantities.

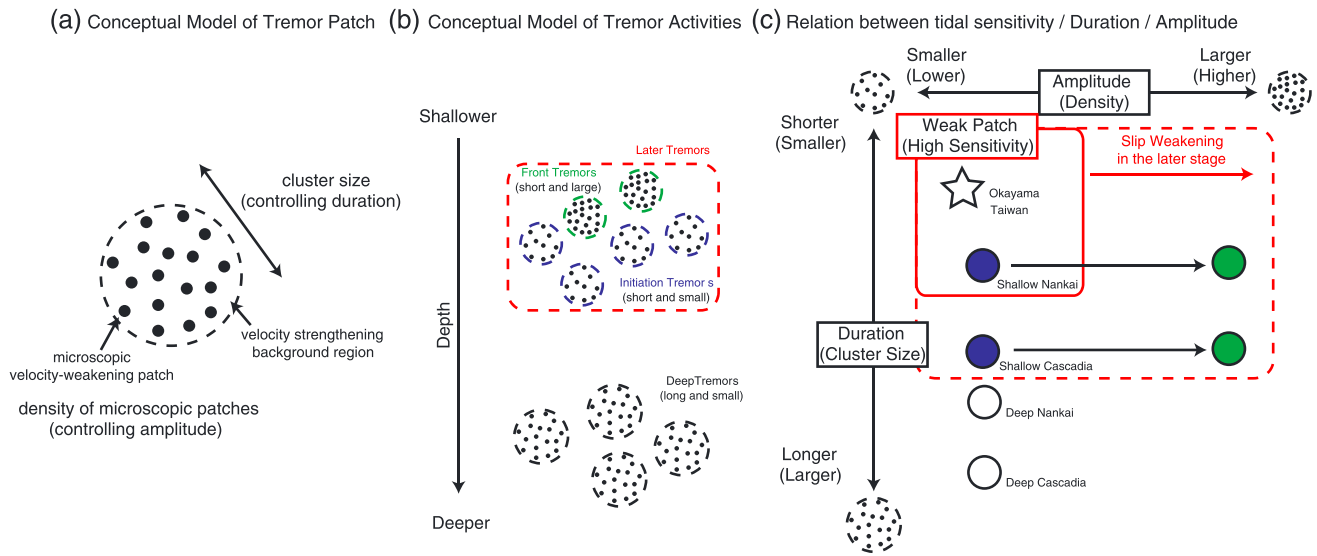


**Figure 9.** Schematic figure of plate interface in transition zone. (a) Conceptual model of tremor patch suggested by Ando *et al.* [2010, 2012] and Nakata *et al.* [2011]. Each small dot represents a microscopic velocity-weakening patch, which is embedded in a velocity-strengthening background region. The size of the cluster (tremor patch) controls duration of tremors. Density of the microscopic velocity-weakening region in the cluster controls amplitude of tremors [Nakata *et al.*, 2011]. (b) Distribution of tremor patches on the plate interface. In shallower parts of the transition zone, the duration of tremors is short (i.e., the cluster size of the tremor patch is small). Both small-amplitude initiation tremors (lower density) and large-amplitude front tremors occur. In the later stage of ETS, both tremors occur as later tremors. In the deeper part, only long-duration and less energetic tremors occur. (c) Schematic relation between tidal sensitivity, duration, and amplitude of tremors. Tremors with short duration and small amplitude, such as initiation tremors in Nankai SZ, cannot bear high stress (i.e., weak patch), resulting in high tidal sensitivity. Stronger large-amplitude tremors, which are not sensitive to tide, occur after the initiation tremors due to the stress accumulation from them. In the later stage of ETS, the plate interface is weakened by slip in the front stage, resulting in the expansion of the tidal-sensitive condition. Deep tremors have long duration, which are strong and not affected by tide.

The second key feature, a negative correlation between duration and tidal sensitivity, could be explained as follows. When cluster size is large, slip on the plate interface lasts for a long duration by the successive breakage of velocity-weakening regions. During the inter-SSE period, these regions within cluster size collectively behave as a large locked area, which is less sensitive to stress change. The opposite is true for short-duration tremors. Hence, long-duration tremors are less sensitive to tides, and high tidal sensitivity is expected only for short tremors.

Ide *et al.* [2015] investigated tidal sensitivity of tremors in Taiwan using the same method as this study without any categorization of tremors, and they found that tidal sensitivity is about  $2 \text{ kPa}^{-1}$  in Taiwan tremors, which is much higher than that estimated in this study for Nankai and Cascadia SZs. Tremors in Taiwan have a median duration of about 18 s. We can also analyze tremors in Okayama prefecture in Nankai SZ, which were investigated by Ide and Tanaka [2014]. Applying the same analysis to their tremor catalog without any categorization of tremors, we found that tidal sensitivity is  $3 \text{ kPa}^{-1}$  for them. Tremors in Okayama prefecture have a median duration of 23 s. These two tremor activities with high tidal sensitivity have a short duration, which is also consistent with the second key feature.

The third key feature, variation among three stages, has been explained by Yabe and Ide [2014] as follows (Figures 9b and 9c). Since the density of velocity-weakening regions controls the local strength of the plate interface, an ETS always starts from a relatively weak region with lower density. Thus, initial tremors may be less energetic. Usually, a high-density region with high strength works as a barrier against the slip in the background region, but it sometimes breaks as well after sufficient tectonic stress accumulation. Once broken, a large energetic slip occurs in this region, probably changing physical conditions around the plate interface. Hence, tidal sensitivity is low during the front stage when a strong tremor patch mainly breaks. Dilatancy strengthening may also reduce tidal sensitivity in the front stage of ETS, and then fluid pressure will diffusively recover in the later stage [e.g., Segall *et al.*, 2010; Liu, 2013]. Alternatively, large stress perturbations due to fast slip in the front stage overwhelm tidal stresses, making them unimportant [Houston, 2015]. It is also possible that the large slip velocity in the SSE front causes a decrease in the

characteristic timescale  $T_a$  of Ader *et al.* [2012], over which stress perturbation is compensated by elastic deformation, to less than the tidal period, resulting in lower tidal sensitivity (Ampuero, 2015, personal communication). Large slip also weakens the plate interface and decreases the strength of velocity-weakening regions, which enhances tidal sensitivity in the later stage of ETSs, which is consistent with the interpretation of Houston [2015]. Healing is presumed to occur after the ETS ends. This study provides further evidence that duration and amplitude of tremors are related to the strength of plate interface (i.e., tidal sensitivity).

In the later stage of ETS, RTRs are triggered as secondary fronts by tidal stress [Houston *et al.*, 2011; Thomas *et al.*, 2013; Royer *et al.*, 2015]. Peng *et al.* [2015] observe rapid tremor migrations near the main front as well. These rapid tremor migrations will be explained as follows in our model. While slow slip propagates in the along-strike direction, the first front passes many tremor patches, which have diverse strength (i.e., diverse amplitude and duration). Weaker patches are broken easily, which outline the propagating front. Meanwhile, stronger patches are less likely to be broken, although it will be broken after some stress accumulation. Once it breaks, it releases higher stress, which accelerates slip, resulting in rapid tremor migrations. If it happens just after the slip pulse reaches the region, it is regarded as the main front, whereas if it happens after the main front has passed, it is regarded as RTRs. The amplitude of tremors in the main front and RTRs is larger [Thomas *et al.*, 2013; Yabe and Ide, 2014], which is consistent with this model.

In addition to tidal sensitivity, duration, and amplitude of tremors, the recurrence intervals of ETSs are also dependent on the along-dip position [Obara *et al.*, 2011; Wech and Creager, 2011]. This fourth key feature suggests that cluster size and density characterizing the frictional heterogeneity on the plate interface are governed by physical quantities, such as temperature, normal pressure, or fluid amount.

Summarizing these observations and interpretations, our schematic model is provided in Figure 9. The frictional heterogeneity on the plate interface is characterized by the cluster size and density of velocity-weakening regions (Figure 9a). On the shallower plate interface, the cluster size is shorter (resulting in a short duration), but the density is more likely to be higher (resulting in large tremor amplitude) (Figure 9b). Large ETSs occur periodically here. They begin with short-duration and small-amplitude tremors (initiation tremors) followed by short-duration and large-amplitude tremors (front tremors), which cause larger slip weakening and energetic tremors, resulting in increase of tidal sensitivity in the later stage of ETSs (Figure 9c). Deeper on the plate interface, cluster size is longer (long duration), but the density is lower (small tremor amplitude) (Figure 9b). Tremors occur more often, but tidal sensitivity is low here because it has higher strength due to the large cluster size (Figure 9c).

A relatively short duration of tremors (Figure 7) and high sensitivity in initiation tremors in Nankai SZ (Figures 4 and 5) suggest that the plate interface in Nankai SZ is generally weaker than in Cascadia SZ. If this is the case, the timescale required for healing might be shorter in Nankai SZ and the strength of the plate interface could recover its original state more easily, resulting in only a small increase of tidal sensitivity during slip in Nankai SZ.

Strong tidal sensitivity of tremors implies that the background slip rate of the plate interface changes with tidal stress, i.e., subducting velocity is faster when tidal stress is larger. This view of unsteady subduction modulated by tidal stress might change the triggering effect of tidal stress to ordinary earthquakes as well. In the traditional view of SZ, the shallower plate interface has strong coupling, which results in large earthquakes, while the plate subducts steadily in the deeper SZ. In this view, tidal stress can only load its stress directly to coupled regions. Because tidal stress (around kilopascal) is much smaller than stress drops of ordinary earthquakes (around megapascal) [e.g., Allmann and Shearer, 2009], the sensitivity of ordinary earthquakes to daily semidiurnal tides is very weak, if any [e.g., Tsuruoka *et al.*, 1995; Cochran *et al.*, 2004]. Meanwhile, in the new view of SZ brought by the discovery of slow earthquakes, unsteady subduction might result in unsteady stress loading in shallower coupling plate interface, that is, sometimes interplate ordinary earthquakes may be more likely to occur, and less likely in other times. Furthermore, the exponential relation between slip velocity and stress also suggests that the effect of a long-term small change of tidal stress amplitude will be enhanced and be more important for the loading to shallower plate interface. It has been suggested that this could explain some long-term variations of ordinary seismicity [Ide and Tanaka, 2014; Tanaka *et al.*, 2015].

## 5. Conclusions

Tectonic tremors in SZs are sensitive to tidal stress. This study investigates the tidal sensitivity of tremors in large tremor activities (ETSs) in Nankai and Cascadia SZs. Tremors are categorized into three types (tremors in the initiation, front, and later stages of ETSs). This study focuses on the spatial variation of tidal sensitivity of these three types of tremors to compare with the spatial variation of other characteristics of tremors, such as duration and amplitude. These characteristics are considered to reflect the heterogeneity on the plate interface. Hence, comparisons between these quantities give insights about the frictional property on the plate interface and the physics of slow earthquakes.

As previous studies suggested, an exponential relation between tremor rate and tidal stress is found. We measure the coefficient in the exponent with the maximum likelihood method and define it as tidal sensitivity, assuming that tremor rate is proportional to slip velocity of surrounding region and this exponential relation represents a rate-and-state friction law, in which the  $a\sigma$  or  $(a - b)\sigma$  value of the law would be related to the tidal sensitivity, considering the period of tidal stressing. Although we interpret the observed exponential relationship as RSF, it can also be interpreted as resulting from a Weibull-type fracture law as suggested by *Houston* [2015]. Tidal sensitivity of tremors is spatially heterogeneous in both the Nankai and Cascadia SZs. Tremors in the initiation stage of ETS have tidal sensitivity in Nankai (about  $0.3 \text{ kPa}^{-1}$  in average,  $1 \text{ kPa}^{-1}$  at highest, corresponding to  $3.3 \text{ kPa}$  and  $1 \text{ kPa}$  for the  $a\sigma$  or  $(a - b)\sigma$  value, respectively), but not in Cascadia (about  $4 \text{ kPa}$  in average). Front tremors have low sensitivity in both SZs. In the later stage of ETS, tidal sensitivity is as high as initiation tremors in Nankai SZ, while sensitivity increases over the course of ETS slip in Cascadia SZ (to about  $2.5 \text{ kPa}$  in average). Tidal sensitivity depends on downdip position. Tremor has higher tidal sensitivity in the shallower ETS zone where short-duration and large-amplitude tremors tend to occur. Meanwhile, tidal sensitivity is lower at deeper depths, where longer-duration and lower-amplitude tremors occur.

Our observations show that the deep plate interface generally follows an exponential-type velocity-strengthening friction law. The increase of tidal sensitivity when large-amplitude tremor occurs suggests that the plate interface is slip weakened by SSEs because the energy rate of tremors is proportional to the moment rate of slip in the region.

Based on the Ando model, we consider that the frictional heterogeneity on the plate interface is characterized by the cluster size and density of the velocity-weakening region. In this context, a larger cluster size results in longer duration and lower tidal sensitivity, which is consistent with observed duration dependency of tidal sensitivity. Higher density represents higher local strength, resulting in larger slip in the front stage of ETS and higher tidal sensitivity in the later stage of ETS, which is consistent with observed tremor amplitude dependency. Along-dip dependency of tremor characteristics suggests that cluster size and density characterizing frictional heterogeneity on the plate interface are controlled by physical quantities affected by depth, such as temperature, normal stress, or fluid amount.

## Appendix A

### A1. Green's Function

We calculate Green's function for a spherical earth for the sake of tidal stress calculation. Here, we assumed that physical properties of the Earth change only in the radial direction and used PREM structure [*Dziewonski and Anderson, 1981*]. To obtain Green's function, we solve the following equation of motion [*Takeuchi and Saito, 1972*]:

$$\begin{aligned}
 (\vec{\nabla} \cdot \tau)_r - \nabla_r(\rho g u) - \rho \nabla_r \Phi + g(\vec{\nabla} \cdot \rho \vec{s}) - \frac{1}{r}(\tau_{r\theta} + \tau_{\phi\phi}) &= \omega^2 \rho u \\
 (\vec{\nabla} \cdot \tau)_\theta - \nabla_\theta(\rho g u) - \rho \nabla_\theta \Phi + \frac{1}{r}(\tau_{r\theta} - \frac{\cos \theta}{\sin \theta} \tau_{\phi\phi}) &= \omega^2 \rho v \\
 (\vec{\nabla} \cdot \tau)_\phi - \nabla_\phi(\rho g u) - \rho \nabla_\phi \Phi + \frac{1}{r}(\tau_{r\phi} + \frac{\cos \theta}{\sin \theta} \tau_{\theta\phi}) &= \omega^2 \rho w
 \end{aligned} \tag{A1}$$

where  $\tau$  is the stress tensor,  $\rho$  is the density before reformation,  $g$  is the initial gravity,  $\Phi$  is the gravity potential change,  $\vec{s} = (u, v, w)$  is the displacement vector, and  $\omega$  is the frequency of tidal loading. The gravity potential change is related to density by

$$\nabla^2 \Phi = 4\pi G \vec{\nabla} \cdot \rho \vec{s} \tag{A2}$$

where  $G$  is the gravitational constant. We also need a constitutive equation between traction and displacement, assuming complete elasticity and isotropy,

$$\begin{aligned}
 \tau_{rr} &= \lambda\varepsilon + 2\mu\frac{\partial u}{\partial r} \\
 \tau_{\theta\theta} &= \lambda\varepsilon + 2\mu\left(\frac{1}{r}\frac{\partial v}{\partial\theta} + \frac{u}{r}\right) \\
 \tau_{\phi\phi} &= \lambda\varepsilon + \frac{2\mu}{r\sin\theta}\left(\frac{\partial w}{\partial\phi} + u\sin\theta + v\cos\theta\right) \\
 \tau_{r\theta} &= \mu\left\{\frac{\partial v}{\partial r} + \frac{1}{r}\left(\frac{\partial u}{\partial\theta} - v\right)\right\} \\
 \tau_{r\phi} &= \mu\left\{\frac{\partial w}{\partial r} + \frac{1}{u\sin\theta}\left(\frac{\partial u}{\partial\phi} - w\sin\theta\right)\right\} \\
 \tau_{\theta\phi} &= \mu\left\{\frac{1}{r}\frac{\partial w}{\partial\theta} + \frac{1}{r\sin\theta}\left(\frac{\partial v}{\partial\phi} - w\cos\theta\right)\right\} \\
 \varepsilon &= \frac{\partial u}{\partial r} + \frac{1}{r}\frac{\partial v}{\partial\theta} + \frac{u}{r} + \frac{1}{r\sin\theta}\left(\frac{\partial w}{\partial\phi} + u\sin\theta + v\cos\theta\right)
 \end{aligned} \tag{A3}$$

To solve equations (A1)–(A3), we expand it using the Legendre polynomial like equation (A4).

$$\begin{aligned}
 u &= \sum_{n=0}^{\infty} \sum_{m=-n}^n U_n(r) Y_{nm}(\theta, \phi) \\
 v &= \sum_{n=0}^{\infty} \sum_{m=-n}^n V_n(r) \frac{\partial Y_{nm}(\theta, \phi)}{\partial\theta} \\
 w &= \sum_{n=0}^{\infty} \sum_{m=-n}^n V_n(r) \frac{\partial Y_{nm}(\theta, \phi)}{\sin\theta\partial\phi} \\
 \tau_{rr} &= \sum_{n=0}^{\infty} \sum_{m=-n}^n T_n^{rr}(r) Y_{nm}(\theta, \phi) \\
 \tau_{r\theta} &= \sum_{n=0}^{\infty} \sum_{m=-n}^n T_n^{r\theta}(r) \frac{\partial Y_{nm}(\theta, \phi)}{\partial\theta} \\
 \tau_{r\phi} &= \sum_{n=0}^{\infty} \sum_{m=-n}^n T_n^{r\phi}(r) \frac{\partial Y_{nm}(\theta, \phi)}{\sin\theta\partial\phi}
 \end{aligned} \tag{A4}$$

$\tau_{\theta\theta}$ ,  $\tau_{\theta\phi}$ , and  $\tau_{\phi\phi}$  can be constructed using  $u$ ,  $v$ ,  $\tau_{rr}$ , and  $\tau_{r\theta}$  if they are given. Gravity potential is also expanded by the Legendre polynomial as follows.

$$\Phi = \sum_{n=0}^{\infty} \Psi_n(r) P_n(\cos\theta) \tag{A5}$$

We also introduce a new parameter  $Q_n$  defined below.

$$Q_n = \frac{\partial\Psi_n}{\partial r} - 4\pi G\rho U_n + \frac{n+1}{r}\Psi_n \tag{A6}$$

Then equations (A1)–(A3) to be solved are rewritten as a first-order system of differential equations with six variables as follows [Takeuchi and Saito, 1972].

$$\begin{aligned}
 \frac{\partial U_n}{\partial r} &= \frac{1}{\lambda + 2\mu} \left[ T_n^{rr} - \frac{\lambda}{r} \{2U_n - n(n+1)V_n\} \right] \\
 \frac{\partial V_n}{\partial r} &= \frac{T_n^{r\theta}}{\mu} + \frac{V_n - U_n}{r} \\
 \frac{\partial T_n^{rr}}{\partial r} &= \frac{2}{r} \left( \lambda \frac{\partial U_n}{\partial r} - T_n^{rr} \right) + \frac{1}{r} \left( \frac{2\lambda + 2\mu}{r} - \rho g \right) \{2U_n - n(n+1)V_n\} + \frac{n(n+1)}{r} T_n^{r\theta} + \rho \left( Q_n - \frac{n+1}{r} \Psi_n - \frac{2g}{r} U_n \right) \\
 \frac{\partial T_n^{r\theta}}{\partial r} &= -\frac{\lambda}{r} \frac{\partial U_n}{\partial r} - \frac{\lambda + 2\mu}{r^2} \{2U_n - n(n+1)V_n\} + \frac{2\mu}{r^2} (U_n - V_n) - \frac{3}{r} T_n^{r\theta} - \frac{\rho}{r} (\Psi_n - gU_n) \\
 \frac{\partial\Psi_n}{\partial r} &= Q_n + 4\pi G\rho U_n - \frac{n+1}{r} \Psi_n \\
 \frac{\partial Q_n}{\partial r} &= \frac{n-1}{r} (Q_n + 4\pi G\rho U_n) + \frac{4\pi G\rho}{r} \{2U_n - n(n+1)V_n\}
 \end{aligned} \tag{A7}$$

The problem is solved with two kinds of boundary condition according to body tide and ocean tide. For body tide, the boundary condition is equation (A8), and that for ocean tide is equation (A9) [Tsuruoka *et al.*, 1995].

$$\begin{aligned}
 U_n(0) &= 0 \\
 V_n(0) &= 0 \\
 T_n^{rr}(a) &= 0 \\
 T_n^{r\theta}(a) &= 0 \\
 \Psi_n(0) &= 0 \\
 Q_n(a) &= \frac{2n+1}{a}
 \end{aligned} \tag{A8}$$

$$\begin{aligned}
 U_n(0) &= 0 \\
 V_n(0) &= 0 \\
 T_n^{rr}(a) &= -\frac{(2n+1)g}{4\pi G a} \\
 T_n^{r\theta}(a) &= 0 \\
 \Psi_n(0) &= 0 \\
 Q_n(a) &= \frac{2n+1}{a}
 \end{aligned} \tag{A9}$$

These differential equations are solved with the code of Okubo and Tsuji [2001] with the Runge-Kutta method, which considers attenuation effect as well.

## A2. Body Tide

Tidal stresses due to body tides are generated by the deformation of the solid Earth produced by the gravitational potential change due to the relative motions of the Moon, Sun, and Earth. The gravitational potential can be expanded in the Legendre polynomials, and only the second and third terms are important in the deformation of the Earth because the distance between the Earth and the Moon or the Sun is sufficiently greater than the radius of the Earth [e.g., Tsuruoka *et al.*, 1995].

Body tides can be calculated as follows using Green's function calculated in the previous section.

$$\begin{aligned}
 \tau_{rr}(r, \theta, \phi, t) &= \sum_{n=2}^3 \Psi_n^{\text{body}}(r, \theta, \phi, t) \times T_n^{rr}(r) \\
 \tau_{r\theta}(r, \theta, \phi, t) &= \sum_{n=2}^3 \frac{\partial \Psi_n^{\text{body}}(r, \theta, \phi, t)}{\partial \theta} \times T_n^{r\theta}(r) \\
 \tau_{r\phi}(r, \theta, \phi, t) &= \sum_{n=2}^3 \frac{\partial \Psi_n^{\text{body}}(r, \theta, \phi, t)}{\sin \theta \partial \phi} \times T_n^{r\theta}(r) \\
 \tau_{\theta\theta}(r, \theta, \phi, t) &= \sum_{n=2}^3 \Psi_n^{\text{body}}(r, \theta, \phi, t) \times \left( \frac{\lambda}{\lambda+2\mu} T_n^{rr}(r) + \frac{2\mu(3\lambda+2\mu)U_n}{\lambda+2\mu} \frac{U_n}{r} \right) + \frac{\partial \Psi_n^{\text{body}}(r, \theta, \phi, t)}{\partial \theta} \times \frac{2\lambda\mu}{\lambda+2\mu} \frac{\cos \theta}{\sin \theta} \frac{V_n(r)}{r} \\
 &\quad + \frac{\partial^2 \Psi_n^{\text{body}}(r, \theta, \phi, t)}{\partial \theta^2} \times \frac{4\mu(\lambda+\mu)V_n(r)}{\lambda+2\mu} \frac{V_n(r)}{r} + \frac{\partial^2 \Psi_n^{\text{body}}(r, \theta, \phi, t)}{\sin^2 \theta \partial \phi^2} \times \frac{2\lambda\mu}{\lambda+2\mu} \frac{V_n(r)}{r} \\
 \tau_{\phi\phi}(r, \theta, \phi, t) &= \sum_{n=2}^3 \Psi_n^{\text{body}}(r, \theta, \phi, t) \times \left( \frac{\lambda}{\lambda+2\mu} T_n^{rr}(r) + \frac{2\mu(3\lambda+2\mu)U_n}{\lambda+2\mu} \frac{U_n}{r} \right) + \frac{\partial \Psi_n^{\text{body}}(r, \theta, \phi, t)}{\partial \theta} \times \frac{4\mu(\lambda+\mu)}{\lambda+2\mu} \frac{\cos \theta}{\sin \theta} \frac{V_n(r)}{r} \\
 &\quad + \frac{\partial^2 \Psi_n^{\text{body}}(r, \theta, \phi, t)}{\partial \theta^2} \times \frac{2\lambda\mu}{\lambda+2\mu} \frac{V_n(r)}{r} + \frac{\partial^2 \Psi_n^{\text{body}}(r, \theta, \phi, t)}{\sin^2 \theta \partial \phi^2} \times \frac{4\mu(\lambda+\mu)}{\lambda+2\mu} \frac{V_n(r)}{r} \\
 \tau_{\theta\phi}(r, \theta, \phi, t) &= \sum_{n=2}^3 \frac{\partial^2 \Psi_n^{\text{body}}(r, \theta, \phi, t)}{\sin \theta \partial \theta \partial \phi} \times \mu \frac{V_n(r)}{r} - \frac{\partial \Psi_n^{\text{body}}(r, \theta, \phi, t)}{\sin \theta \partial \phi} \times \mu \frac{\cos \theta}{\sin \theta} \frac{V_n(r)}{r}
 \end{aligned} \tag{A10}$$

In each mode of the polynomial, the temporal change of the gravitational potential  $\Psi_n^{\text{body}}(r, \theta, \phi, t)$  can be expressed as the summation of various tidal constituents, whose frequency can be represented by the combination of six fundamental frequencies, whose coefficient is called Doodson's number. In our calculation, the tidal potential listed in Tamura [1987] is used.

### A3. Ocean Tide

Tidal stresses due to ocean tides are generated by the mass loading of ocean water on the Earth's surface. The gravitational potential change, which causes the body tides, also triggers the movement of ocean water, which then produces the stress change in the solid Earth. The temporal change of sea surface height is predicted from oceanography. SPOTL [Agnew, 2012] calculates such time series using a given ocean model. We used ocean models listed in Table 1 as an input for SPOTL. We used 10 major tidal constituents (K1, K2, M2, N2, O1, P1, Q1, S2, mf, and mm), eight of which are short-period tides and the remainder long-period tides. By multiplying the sea surface height change with Green's function for point mass loading at the surface and integral over the surface, we obtain the tidal stress due to ocean tide, as in equation (A11).

$$\tau_{ij}(r, \theta, \phi, t) = \int H(\theta', \phi', t) R_{ijkl}(\theta, \phi, \theta', \phi') \tau'_{kl}(r, \theta, \phi, \theta', \phi') d\theta' d\phi' \quad (\text{A11})$$

where  $R_{ijkl}(\theta, \phi, \theta', \phi')$  is a rotation tensor to change coordinates and  $\tau'_{kl}$  is Green's function for point loading on the surface,

$$\begin{aligned} \tau'_{rr} &= \frac{G}{a} \sum_{n=2}^{\infty} T_n^{rr}(r) P_n(\cos \vartheta) \\ \tau'_{r\theta} &= \frac{G}{a} \sum_{n=2}^{\infty} T_n^{r\theta}(r) \frac{\partial P_n(\cos \vartheta)}{\partial \vartheta} \\ \tau'_{\theta\theta} &= \frac{G}{a} \sum_{n=2}^{\infty} T_n^{rr}(r) P_n(\cos \vartheta) - 2\mu \frac{\partial U_n(r)}{\partial r} P_n(\cos \vartheta) + 2\mu \left( \frac{V_n(r) \partial^2 P_n(\cos \vartheta)}{r \partial \vartheta^2} + \frac{U_n(r)}{r} P_n(\cos \vartheta) \right) \\ \tau'_{\phi\phi} &= \frac{G}{a} \sum_{n=2}^{\infty} T_n^{rr}(r) P_n(\cos \vartheta) - 2\mu \frac{\partial U_n(r)}{\partial r} P_n(\cos \vartheta) + 2\mu \left( \frac{U_n(r)}{r} P_n(\cos \vartheta) - \frac{\cos \vartheta}{r \sin \vartheta} V_n(r) \frac{\partial P_n(\cos \vartheta)}{\partial \vartheta} \right) \end{aligned} \quad (\text{A12})$$

where  $\vartheta(\theta, \phi, \theta', \phi')$  is an angular distance between  $(\theta, \phi)$  and  $(\theta', \phi')$ . To calculate infinite summations in equation (A12) accurately, we divide the infinite summation into two parts as in Okubo [1988]. An example for  $\tau'_{rr}$  in the case of  $r < a$  is shown below.

$$\begin{aligned} \tau'_{rr} &= \sum_{n=2}^{\infty} T_n^{rr}(r) P_n(\cos \vartheta) \\ &= \sum_{n=2}^{\infty} N_n n^2 \left( \frac{r}{a} \right)^n P_n(\cos \vartheta) \\ &= N_{\infty} \sum_{n=2}^{\infty} n^2 \left( \frac{r}{a} \right)^n P_n(\cos \vartheta) + \sum_{n=2}^{\infty} (N_n - N_{\infty}) n^2 \left( \frac{r}{a} \right)^n P_n(\cos \vartheta) \end{aligned} \quad (\text{A13})$$

In the numerical calculation, we calculate  $N_n$  up to  $n = 45,000$ , and  $N_{\infty}$  is replaced by  $N_{45,000}$ . The generating function is substituted in  $\sum_{n=2}^{\infty} n^2 \left( \frac{r}{a} \right)^n P_n(\cos \vartheta)$ . The second term in equation (A13) is summed up to  $n = 45,000$ . For the integration of equation (A11), we used a finer mesh ( $\sim 0.5 \text{ km} \times \sim 0.5 \text{ km}$ ) around the origin, where tidal stress is calculated, and a coarser mesh ( $\sim 20 \text{ km} \times \sim 20 \text{ km}$ ) if further than 100 km from the origin. Land-sea distribution is distinguished with a  $1/64^\circ$  grid in the SPOTL [Agnew, 2012]. We integrate ocean loads over 500 km from the origin.

### A4. Plate Model

We can calculate the tidal stress tensor by specifying the location (latitude, longitude, and depth) and time. Because slow earthquakes occur on the plate interface [e.g., Dragert et al., 2001; Ide et al., 2007a; Ito et al., 2007; Shelly et al., 2007a], we calculate the tidal stress tensor on the inferred plate interface. We used the plate model by Baba et al. [2002], Nakajima and Hasegawa [2007], and Hirose et al. [2008] for the Nankai subduction zone and McCrory et al. [2012] for Cascadia. We interpolate these models into  $0.01^\circ$  grids and calculate strike and dip of the fault on each grid. We calculate tidal stress tensor at every  $0.1^\circ$  grid points.

To convert the stress tensor to traction (normal stress, slip-parallel shear stress, and slip-orthogonal shear stress) on the plate interface, we need the strike, dip, and rake of the slip vector on the plate interface. We calculate strike and dip from the interpolated plate models. Rake is calculated so that the horizontal components of a slip vector on the plate interface are consistent with the motion vector of the subducting oceanic plate at that location. Relative plate motion is calculated using DeMets et al. [2010].

## Acknowledgments

We thank Amanda Thomas and an anonymous reviewer for their helpful comments to improve this manuscript. We also thank J. P. Ampuero for helpful suggestions on applying the RSF model of Ader *et al.* [2012]. For the computation of tidal stress, we have used the computer systems of the Earthquake and Volcano Information Center of the Earthquake Research Institute, the University of Tokyo (<http://www.eic.eri.u-tokyo.ac.jp/computer/manual/eic2015/index.php?English>). The tremor data for this paper were constructed using seismic data from the National Research Institute for Earth Science and Disaster Prevention (<http://www.bosai.go.jp/e/>) and from Incorporated Research Institutions for Seismology (<http://www.iris.edu/hq/>) (see Yabe and Ide [2014] for more details). As a part of tidal stress calculation, SPOTL [Agnew, 2012] was used (<http://igppweb.ucsd.edu/~agnew/Spotl/spotlmain.html>). The EOT11a model used in this study is computed based on altimetry missions operated by CNES/NASA (TOPEX, Jason-1), ESA (ERS-1/2, Envisat, Cryosat-2), US Navy/NOAA (GFO), CNES/NASA/Eumetsat/NOAA (Jason-2), and ISRO/CNES (Saral). The data are provided by AVISO, ESA, NOAA, and PODAAC. Ocean models including EOT11a are downloaded from SPOTL. GMT software [Wessel and Smith, 1998] is used to draw figures. This work was supported by JSPS KAKENHI grants 14J08291 and 23244090 and by the Program for Leading Graduate Schools, MEXT, Japan.

## References

- Ader, T. J., J.-P. Ampuero, and J.-P. Avouac (2012), The role of velocity-neutral creep on the modulation of tectonic tremor activity by periodic loading, *Geophys. Res. Lett.*, *39*, L16310, doi:10.1029/2012GL052326.
- Agnew, D. C. (2012), SPOTL: Some Programs for Ocean-Tide Loading, SIO Technical Report, Scripps Institution of Oceanography.
- Allmann, B. P., and P. M. Shearer (2009), Global variations of stress drop for moderate to large earthquakes, *J. Geophys. Res.*, *114*, B01310, doi:10.1029/2008JB005821.
- Ando, R., R. Nakata, and T. Hori (2010), A slip pulse model with fault heterogeneity for low-frequency earthquakes and tremor along plate interfaces, *Geophys. Res. Lett.*, *37*, L10310, doi:10.1029/2010GL043056.
- Ando, R., N. Takeda, and T. Yamashita (2012), Propagation dynamics of seismic and aseismic slip governed by fault heterogeneity and Newtonian rheology, *J. Geophys. Res.*, *117*, B11308, doi:10.1029/2012JB009532.
- Audet, P., M. G. Bostock, N. I. Christensen, and S. M. Peacock (2009), Seismic evidence for overpressured subducted oceanic crust and megathrust fault sealing, *Nature*, *457*, 76–78, doi:10.1038/nature07650.
- Baba, T., Y. Tanioka, P. R. Cummins, and K. Uehira (2002), The slip distribution of the 1946 Nankai earthquake estimated from tsunami inversion using a new plate model, *Phys. Earth Planet. Inter.*, *132*, 59–73, doi:10.1016/S0031-9201(02)00044-4.
- Beeler, N. M., A. Thomas, R. Bürgmann, and D. Shelly (2013), Inferring fault rheology from low-frequency earthquakes on the San Andreas, *J. Geophys. Res. Solid Earth*, *118*, 5976–5990, doi:10.1002/2013JB010118.
- Cochran, E. S., J. E. Vidale, and S. Tanaka (2004), Earth tides can trigger shallow thrust fault earthquakes, *Science*, *306*, 1164–1166, doi:10.1126/science.1103961.
- DeMets, C., R. G. Gordon, and D. F. Argus (2010), Geologically current plate motions, *Geophys. J. Int.*, *181*, 1–80, doi:10.1111/j.1365-246X.2009.04491.x.
- Dieterich, J. (1994), A constitutive law for rate of earthquake production and its application to earthquake clustering, *J. Geophys. Res.*, *99*, 2601–2618, doi:10.1029/93JB02581.
- Dieterich, J. H. (1978), Time-dependent friction and the mechanics of stick-slip, *Pure Appl. Geophys.*, *116*, 790–806, doi:10.1007/BF00876539.
- Dragert, H., K. Wang, and T. S. James (2001), A silent slip event on the deeper Cascadia subduction interface, *Science*, *292*(5521), 1525–1528, doi:10.1126/science.1060152.
- Dziewonski, A. M., and A. Anderson (1981), Preliminary reference Earth model, *Phys. Earth Planet. Inter.*, *25*, 297–356, doi:10.1016/0031-9201(81)90046-7.
- Egbert, G. D., and S. Y. Erofeeva (2002), Efficient inverse modeling of barotropic ocean tides, *J. Atmos. Oceanic Technol.*, *19*, 183–204.
- Guo, X., S. M. Varlamov, and Y. Miyazawa (2010), Coastal ocean modeling by the nesting method, *Bull. Coast. Oceanogr.*, *47*(2), 113–123.
- Hawthorne, J. C., and A. M. Rubin (2010), Tidal modulation of slow slip in Cascadia, *J. Geophys. Res.*, *115*, B09406, doi:10.1029/2010JB007502.
- Hawthorne, J. C., and A. M. Rubin (2013), Tidal modulation and back-propagating fronts in slow slip events simulated with a velocity-weakening to velocity-strengthening friction law, *J. Geophys. Res. Solid Earth*, *118*, 1216–1239, doi:10.1002/jgrb.50107.
- Hirose, F., J. Nakajima, and A. Hasegawa (2008), Three-dimensional seismic velocity structure and configuration of the Philippine Sea slab in southwestern Japan estimated by double-difference tomography, *J. Geophys. Res.*, *113*, B09315, doi:10.1029/2007JB005274.
- Houston, H. (2015), Low friction and fault weakening revealed by rising sensitivity of tremor to tidal stress, *Nat. Geosci.*, *8*(5), 409–415, doi:10.1038/ngeo2419.
- Houston, H., B. G. Delbridge, A. G. Wech, and K. C. Creager (2011), Rapid tremor reversals in Cascadia generated by a weakened plate interface, *Nat. Geosci.*, *4*, 404–409, doi:10.1038/ngeo1157.
- Ide, S. (2010), Striations, duration, migration, and tidal response in deep tremor, *Nature*, *466*, 356–359, doi:10.1038/nature09251.
- Ide, S. (2012), Variety and spatial heterogeneity of tectonic tremor worldwide, *J. Geophys. Res.*, *117*, B03302, doi:10.1029/2011JB008840.
- Ide, S., and Y. Tanaka (2014), Controls on plate motion by oscillating tidal stress: Evidence from deep tremors in western Japan, *Geophys. Res. Lett.*, *41*, 3842–3850, doi:10.1002/2014GL060035.
- Ide, S., and S. Yabe (2014), Universality of slow earthquakes in the very low frequency band, *Geophys. Res. Lett.*, *41*, 2786–2793, doi:10.1002/2014GL059712.
- Ide, S., D. R. Shelly, and G. C. Beroza (2007a), Mechanism of deep low frequency earthquakes: Further evidence that deep non-volcanic tremor is generated by shear slip on the plate interface, *Geophys. Res. Lett.*, *34*, L03308, doi:10.1029/2006GL028890.
- Ide, S., G. C. Beroza, D. R. Shelly, and T. Uchide (2007b), A scaling law for slow earthquakes, *Nature*, *447*(7140), 76–79, doi:10.1038/nature05780.
- Ide, S., S. Yabe, H. J. Tai, and K. H. Chen (2015), Thrust type-focal mechanisms of tectonic tremors in Taiwan: Evidence of subduction, *Geophys. Res. Lett.*, doi:10.1002/2015GL063794, in press.
- Idehara, K., S. Yabe, and S. Ide (2014), Regional and global variations in the temporal clustering of tectonic tremor activity, *Earth Planet. Space*, *66*, 66, doi:10.1186/1880-5981-66-66.
- Ito, Y., K. Obara, K. Shiomi, S. Sekine, and H. Hirose (2007), Slow earthquakes coincident with episodic tremors and slow slip events, *Science*, *315*, 503–506, doi:10.1126/science.1134454.
- Liu, C., A. T. Linde, and I. S. Sacks (2009), Slow earthquakes triggered by typhoons, *Nature*, *459*(7248), 833–836, doi:10.1038/nature08042.
- Liu, Y. (2013), Numerical simulations on megathrust rupture stabilized under strong dilatancy strengthening in slow slip region, *Geophys. Res. Lett.*, *40*, 1311–1316, doi:10.1002/grl.50298.
- Marone, C. (1998), Laboratory-derived friction laws and their application to seismic faulting, *Annu. Rev. Earth Planet. Sci.*, *26*(1), 643–696, doi:10.1146/annurev.earth.26.1.643.
- Matsumoto, K., T. Takanezawa, and M. Ooe (2000), Ocean tide models developed by assimilating Topex/Poseidon altimeter data into hydrodynamical model: A global model and a regional model around Japan, *J. Oceanogr.*, *56*, 567–581.
- McCrorry, P. A., J. L. Blair, F. Waldhauser, and D. H. Oppenheimer (2012), Juan de Fuca slab geometry and its relation to Wadati-Benioff zone seismicity, *J. Geophys. Res.*, *117*, B09306, doi:10.1029/2012JB009407.
- Miyazawa, M., and J. Mori (2005), Detection of triggered deep low frequency events from the 2003 Tokachi-oki earthquake, *Geophys. Res. Lett.*, *32*, L10307, doi:10.1029/2005GL022539.
- Nakajima, J., and A. Hasegawa (2007), Subduction of the Philippine Sea plate beneath southwestern Japan: Slab geometry and its relationship to arc magmatism, *J. Geophys. Res.*, *112*, B08306, doi:10.1029/2006JB004770.
- Nakata, R., N. Suda, and H. Tsuruoka (2008), Non-volcanic tremor resulting from the combined effect of earth tides and slow slip events, *Nat. Geosci.*, *1*, 676–678, doi:10.1038/ngeo288.
- Nakata, R., R. Ando, T. Hori, and S. Ide (2011), Generation mechanism of slow earthquakes: Numerical analysis based on a dynamic model with brittle-ductile mixed fault heterogeneities, *J. Geophys. Res.*, *116*, B08308, doi:10.1029/2010JB008188.
- Obara, K. (2002), Nonvolcanic deep tremor associated with subduction in southwest Japan, *Science*, *296*(5573), 1679–1681, doi:10.1126/science.1070378.

- Obara, K., H. Hirose, F. Yamamizu, and K. Kasahara (2004), Episodic slow slip events accompanied by non-volcanic tremors in southwest Japan subduction zone, *Geophys. Res. Lett.*, *31*, L23602, doi:10.1029/2004GL020848.
- Obara, K., T. Matsuzawa, S. Tanaka, T. Kimura, and T. Maeda (2011), Migration properties of non-volcanic tremor in Shikoku, south-west Japan, *Geophys. Res. Lett.*, *38*, L09311, doi:10.1029/2011GL047110.
- Ogata, Y. (1983), Estimation of the parameters in the modified Omori formula for aftershock frequencies by the maximum likelihood procedure, *J. Phys. Earth*, *31*, 115–124, doi:10.4294/jpe1952.31.115.
- Okubo, S. (1988), Asymptotic solutions to the static deformation of the Earth—I. Spheroidal mode, *Geophys. J. Int.*, *92*, 39–51, doi:10.1111/j.1365-246X.1988.tb01119.x.
- Okubo S., and D. Tsuji (2001), Complex Green's function for diurnal/semidiurnal loading problems, *J. Geod. Soc. Jpn.*, *47*, 225–230, doi:10.11366/sokuchi1954.47.225.
- Peng, Y., A. M. Rubin, M. G. Bostock, and J. G. Armbruster (2015), High-resolution imaging of rapid tremor migrations beneath southern Vancouver Island using cross-station cross correlations, *J. Geophys. Res. Solid Earth*, *120*, doi:10.1002/2015JB011892.
- Rogers, G., and H. Dragert (2003), Episodic tremor and slip on the Cascadia subduction zone: The chatter of silent slip, *Science*, *300*, 1942–1943, doi:10.1126/science.1084783.
- Royer, A. A., A. M. Thomas, and M. G. Bostock (2015), Tidal modulation and triggering of low-frequency earthquakes in northern Cascadia, *J. Geophys. Res. Solid Earth*, *120*, doi:10.1002/2014JB011430.
- Rubin, A. M. (2011), Designer friction laws for bimodal slow slip propagation speeds, *Geochem. Geophys. Geosyst.*, *12*, Q04007, doi:10.1029/2010GC003386.
- Rubinstein, J. L., J. E. Vidale, J. Gombert, P. Bodin, K. C. Creager, and S. D. Malone (2007), Non-volcanic tremor driven by large transient shear stresses, *Nature*, *448*, 579–582, doi:10.1038/nature06017.
- Rubinstein, J. L., M. La Rocca, J. E. Vidale, K. C. Creager, and A. G. Wech (2008), Tidal modulation of nonvolcanic tremor, *Science*, *319*, 186–189, doi:10.1126/science.1150558.
- Savcenko, R., and W. Bosch (2012), EOT11a—Empirical ocean tide model from multi-mission satellite altimetry. DGF1 Report No. 89.
- Segall, P., A. M. Rubin, A. M. Bradley, and J. R. Rice (2010), Dilatant strengthening as a mechanism for slow slip events, *J. Geophys. Res.*, *115*, B12305, doi:10.1029/2010JB007449.
- Shelly, D. R., G. C. Beroza, S. Ide, and S. Nakamura (2006), Low-frequency earthquakes in Shikoku, Japan, and their relationship to episodic tremor and slip, *Nature*, *442*, 188–191, doi:10.1038/nature04931.
- Shelly, D. R., G. C. Beroza, and S. Ide (2007a), Non-volcanic tremor and low-frequency earthquake swarms, *Nature*, *446*(7133), 305–307, doi:10.1038/nature05666.
- Shelly, D. R., G. C. Beroza, and S. Ide (2007b), Complex evolution of transient slip derived from precise tremor locations in western Shikoku, Japan, *Geochem. Geophys. Geosyst.*, *8*, Q10014, doi:10.1029/2007GC001640.
- Takeuchi, H., and M. Saito (1972), Seismic surface waves, in *Seismology: Surface Waves and Earth Oscillations, Methods in Comput. Phys.*, vol. 11, edited by B. A. Bolt, pp. 217–295, Academic, New York.
- Tamura, Y. (1987), A harmonic development of the tide-generating potential, *Bull. Inf. Marées Terrestres*, *99*, 6813–6855.
- Tanaka, S. (2010), Tidal triggering of earthquakes precursory to the recent Sumatra megathrust earthquakes of 26 December 2004 (Mw 9.0), 28 March 2005 (Mw 8.6), and 12 September 2007 (Mw 8.5), *Geophys. Res. Lett.*, *37*, L02301, doi:10.1029/2009GL041581.
- Tanaka, S. (2012), Tidal triggering of earthquakes prior to the 2011 Tohoku-Oki earthquake (Mw 9.1), *Geophys. Res. Lett.*, *39*, L00G26, doi:10.1029/2012GL051179.
- Tanaka, Y., S. Yabe, and S. Ide (2015), An estimate of tidal and non-tidal modulations of plate subduction speed in the transition zone in the Tokai district, *Earth Planets Space*, *67*, 141, doi:10.1186/s40623-015-0311-2.
- Thomas, A. M., R. M. Nadeau, and R. Bürgmann (2009), Tremor-tide correlations and near-lithostatic pore pressure on the deep San Andreas fault, *Nature*, *462*, 1048–1051, doi:10.1038/nature08654.
- Thomas, A. M., R. Bürgmann, D. R. Shelly, N. M. Beeler, and M. L. Rudolph (2012), Tidal triggering of low frequency earthquakes near Parkfield, California: Implications for fault mechanics within the brittle-ductile transition, *J. Geophys. Res.*, *117*, B05301, doi:10.1029/2011JB009036.
- Thomas, T. W., J. E. Vidale, H. Houston, K. C. Creager, J. R. Sweet, and A. Ghosh (2013), Evidence for tidal triggering of high-amplitude rapid tremor reversals and tremor streaks in northern Cascadia, *Geophys. Res. Lett.*, *40*, 4254–4259, doi:10.1002/grl.50832.
- Tsuruoka, H., M. Ohtake, and H. Sato (1995), Statistical test of the tidal triggering of earthquakes: Contribution of the ocean tide loading effect, *Geophys. J. Int.*, *122*, 183–194.
- Watanabe, T., Y. Hiramatsu, and K. Obara (2007), Scaling relationship between the duration and the amplitude of non-volcanic deep low-frequency tremors, *Geophys. Res. Lett.*, *34*, L07305, doi:10.1029/2007GL029391.
- Wech, A. G., and K. C. Creager (2011), A continuum of stress, strength and slip in the Cascadia subduction zone, *Nat. Geosci.*, *4*, 624–628, doi:10.1038/ngeo1215.
- Wessel, P., and W. H. F. Smith (1998), New, improved version of generic mapping tools released, *Eos Trans. AGU*, *79*(47), 579, doi:10.1029/98EO00426.
- Yabe, S., and S. Ide (2014), Spatial distribution of seismic energy rate of tectonic tremors in subduction zones, *J. Geophys. Res. Solid Earth*, *119*, 8171–8185, doi:10.1002/2014JB011383.